

**Exploring the Affinity and Selectivity of Sedimentary Mackinawite (FeS)
Towards Natural Organic Matter**

Kathryn Balind

A Thesis in The Department of Chemistry and Biochemistry

Presented in Partial Fulfillment of the Requirements
for the Degree of Master of Science (Chemistry)
at Concordia University
Montréal, Québec, Canada

March 2019

©Kathryn Balind, 2019

CONCORDIA UNIVERSITY
School of Graduate Studies

This is to certify that the thesis prepared

By: Kathryn Balind

Entitled: Exploring the Affinity and Selectivity of Sedimentary Mackinawite (FeS) Towards Natural Organic Matter

and submitted in partial fulfillment of the requirements for the degree of

Master of Science (Chemistry)

complies with the regulations of the University and meets the accepted standards with respect to originality and quality.

Signed by the final Examining Committee:

Chair

Examiner

Dr. Xavier Ottenwaelder

Examiner

Dr. Rafik Naccache

Supervisor

Dr. Yves Gélinas

Approved by _____
Chair of Department or Graduate Program Director

2019

Dean of Faculty

Abstract

Exploring the Affinity and Selectivity of Sedimentary Mackinawite (FeS) Towards Natural Organic Matter

Kathryn Balind

Concordia University 2019

MSc Thesis

The biogeochemical cycle of sulfur is intimately linked with those of carbon and iron through the formation of iron-sulfur complexes. Iron-sulfide minerals such as mackinawite (FeS) and greigite (Fe_3S_4) form under anoxic conditions in marine and lacustrine sediments. Reactive ferric iron oxide species, abundant in oxic surface sediments, can undergo reductive dissolution at the oxic-anoxic interface leading to the formation of soluble $\text{Fe}(\text{II})$ which can then precipitate in the form of iron sulfide species. While iron-oxides have been thoroughly explored in terms of their ability to sorb and sequester organic carbon (OC) in sediments (Lalonde et al., 2012), the role of FeS in the long-term sequestration of OC remains poorly defined. In this study, we present depth concentration profiles for dissolved OC, iron, and sulfur in the liquid-phase (pore water) along with speciation data from sequential extractions of sulfur in the solid-phase collected from sediment cores from the St. Lawrence Estuary and the Saguenay Fjord, indicating possible evidence of FeS -promoted OC sequestration in sediments, the only sink for atmospheric CO_2 on a geological time scale. Additionally, we present synthetic iron-sulfide mineral sorption experiments using natural organic matter (NOM) in order to assess the importance of FeS in sedimentary OC storage. Scanning electron microscopy shows that NOM influences the size and surface area of FeS aggregates, therefore also influencing their reactivity. The effect of NOM on the reactivity of FeS towards re-oxidation was explored using a modified dithionite-citrate buffer reduction method (1) for both dry and wet synthetic FeS minerals. Characterization of the synthetically prepared FeS -NOM complexes and specific anoxic sediments was carried out using synchrotron x-ray techniques, which also show the functional groups of the NOM which preferentially bind to FeS . This study shows for the first time that FeS plays an active role in sedimentary OC preservation.

Acknowledgements

My utmost appreciation goes to my supervisor, Dr. Yves Gélinas, who gave me a chance as an undergraduate student, and supported me throughout these years as a graduate student. He has contributed to my growth as a scientist by supporting my curious nature and unique way of seeing.

I would also like to thank the previous lab members whose shoulders I feel I am standing on: Dr. Andrew Barber and Dr. Karine Lalonde, for their work on iron oxide promoted carbon preservation in sediment.

I would like to thank my parents, brother, and friends for their ongoing support and words of encouragement, as well as my colleagues Anic Imfeld, Aleshia Kormendi, Frederic Leone, Frederic Seguin, Alex Tétrault, Kwan Ming Tam, Aude Flamand, and past lab members Amanda Gabriel, Mina Ibrahim, Azadeh Joshani, and Anja Moritz.

Contributions of Authors

This manuscript was written by Kathryn Balind, edited by Dr. Yves Gélinas, with helpful input from Anic Imfeld and Gabi Mandl. On board chemical analysis of sediment and pore water from the sampling missions was done by Kathryn Balind with valuable assistance from Dr. Andrew Barber in 2017, and from Alex Tétrault in 2018. Alex Tétrault also carried out ICP-MS analysis for total dissolved Mn and Fe in the sediment pore water from the 2018 mission. The remaining chemical analyses, as well as synthetic experiments for SEM analysis and isotherms were carried out by Kathryn Balind. The samples for STXM/NEXAFS analysis were prepared in our lab and shipped (anoxically) to Dr. Aude Picard who carried out the synchrotron analysis and data treatment. The experiments using the DCB method to quantify mackinawite oxidation were performed by both Kathryn Balind and Alex Tétrault.

Contents

List of Figures	vi
List of Tables	viii
1 Introduction	1
1.1 Sediment Chemistry and Composition	2
1.2 Chemical Cycles of C, O, Fe, and S in Sediment	6
1.3 Carbon Preservation by Iron Oxides in Sediment.....	9
1.4 Sulfidation of Iron Oxides and the Precipitation of Iron Sulfides in Sediment.....	12
1.5 Iron Monosulfide (“Mackinawite”) and Organic Matter	14
1.6 Objective and Arrangement of Thesis	16
2 Materials and Methods.....	17
2.1 Sediment Sampling and Analysis	17
2.1.1 Study Area.....	17
2.1.2 Removal of Sediment from the St. Lawrence River and Saguenay Fjord	19
2.1.3 Chemical Analysis of Pore Water	20
2.1.4 Chemical Analysis of Solid-Phase	21
2.2 Isotherms.....	21
2.2.1 Sources and Treatment of Organic Matter	21
2.2.2 Precipitation and Analysis of FeS	21
2.2.3 Calculation of Binding Coefficients from Isotherms	22
2.3 Scanning Electron Microscopy.....	24
2.4 Dithionite-Citrate Buffer Reduction (DCB) Method.....	25
2.5 Synchrotron X-ray	25
3 Results.....	26
3.1 Chemical Speciation Profiles for the Saguenay Fjord and St. Lawrence Estuary.....	26
3.2 Sorption and Co-precipitation of NOM on Synthetic FeS	30
3.2.1 Sorption Isotherms and Constants.....	30
3.2.2 Comparison of Error Function Values	35
3.3 Characterization of FeS Precipitates by Scanning Electron Microscopy (SEM)	35
3.4 Effect of Associated OM on FeS Oxidation	37
3.5 Characterization of Molecular Binding of OM on FeS	38

3.5.1	Synthetic FeS Precipitated with OM	38
3.5.2	Anoxic Sediment Samples	41
4	Discussion.....	42
4.1	Sorption Between NOM and FeS	42
4.2	The Effect of OM on FeS Aggregation	46
4.3	The Effect of NOM on FeS Reactivity Towards O ₂	47
4.4	Surface Chemistry of FeS and NOM.....	48
5	Conclusions and Future Work.....	49
	References	51

List of Figures

Figure 1.1:	pH measurements taken between year 1930 and 2010 from the Lower St. Lawrence Estuary with a 95% confidence interval. Samples were collected at a depth between 170-335m. The number in parenthesis represents the number of data points. Figure modified from Mucci et al., 2011 (2).	1
Figure 1.2:	A simplified version of the carbon cycle showing the amount of organic carbon in Pg stored in each of the Earth's reservoirs (3). Figure modified from Canuel et al., 2012 (4).	2
Figure 1.3:	Pourbaix (pH-Eh) diagram for dissolved iron species in an inorganic seawater solution. Image sourced from Rickard and Luther, 2007 (5).	4
Figure 1.4:	A simplified representation of the relative abundance of dissolved redox-active species in the sediment profile, from the sediment-water interface to depth. Image sourced from Rickard and Luther, 2007 (5).	8
Figure 1.5:	Pourbaix diagram showing the speciation of dissolved iron-monosulfide at activities of iron and sulfur that approach those found in natural systems. In marine conditions, aqueous mackinawite is expected to exist at FeS _{aq} . Image sourced from Rickard and Luther, 2007 (5).	14
Figure 2.1:	A map showing the geographical location of the St. Lawrence River and Saguenay Fjord. The difference in environment for stations SAG-05 and STN-23 are apparent; OM at SAG-05 is more of a terrestrial origin, compared to the more marine origin at STN-23.	17
Figure 2.2:	The profile for reduction potential from the sediment at station SAG-05 collected during past sampling missions in 2000 and 2001.	18
Figure 2.3:	The box-core of sediment removed at station SAG-05 shows the obvious transition from oxic sediment (top) to anoxic (sulfidic) sediment at the bottom.	19

Figure 3.1:	Sediment profiles for station SAG-05. The data was acquired for this study during the summers of 2017 and 2018. Additional data was added to this figure from sampling missions in 2000, 2001, and 2002. Note the labels for SO_4^{2-} and HS^- . $[\text{Fe}]_d$ consists of dissolved Fe(II) and Fe(III).	27
Figure 3.2:	Liquid and solid-phase profiles for STN-23 from sampling missions during the summers of 2017 and 2018. Data from older years (past missions-data obtained by past students) added. Note the labels for SO_4^{2-} and HS^- . $[\text{Fe}]_d$ consists of dissolved Fe(II) and Fe(III).	28
Figure 3.3:	Adsorption and co-precipitation isotherms from the experimental data showing the amount of DOC sorbed by FeS for corn, soil and plankton OM.	31
Figure 3.4:	The experimental sorption isotherms compared to the Langmuir, Freundlich, and Redlich-Peterson model isotherms (see legend at right). The x-axis in the above graphs shows C_e (mg/L), the concentration of DOC in solution at equilibrium with FeS, and the y-axis shows Q_e (mg/g), the mass of DOC associated to the FeS precipitate.	33
Figure 3.5:	Scanning electron microscopy images of synthetic FeS. Panels A to C are of FeS precipitated in the absence of OM, and panels D to F are of FeS precipitated in the presence of a 40 μM soil OM leachate.	36
Figure 3.6:	The change in Fe(II) oxidized after exposure to atmospheric O ₂ , precipitated with varying concentrations of OM. The x-axis is presented as a logarithmic scale of the amount of OC measured in the precipitate and the y-axis shows the amount of Fe released per g of FeS.	37
Figure 3.7:	STXM/NEXAFS maps for the synthetically prepared FeS with planktonic OM by methods of co-precipitation (A) and adsorption (B). Samples were dried under N ₂ in the glove box and transported for analysis anoxically. The same region on the particle was examined for Fe and each C functionality. The brightest regions on the images are spots of strongest absorption. The white bar represents 1 μm .	39
Figure 3.8:	The NEXAFS spectrum of the Fe L _{III} -edge of synthetic FeS co-precipitated with NOM (A), compared to the spectra of the reference compounds (B); Mackinawite (FeS), Vivianite ($\text{Fe}_2+\text{Fe}_2+2(\text{PO}_4)_2 \cdot 8\text{H}_2\text{O}$), and Siderite (FeCO_3), which are all commonly found in sediments and contain Fe(II).	40
Figure 3.9:	STXM/NEXAFS maps for anoxic sediment from two stations, SAG-05 (A,B) and STN-23 (C,D) showing distribution of ferrous iron, ferric iron, and carboxylic C in the sample. Images on the top row (A,C) were obtained at the American Light Source (ALS) in California, USA, and images on the bottom row (B,D) were obtained at the Canadian Light Source (CLS) in Saskatchewan, Canada.	41

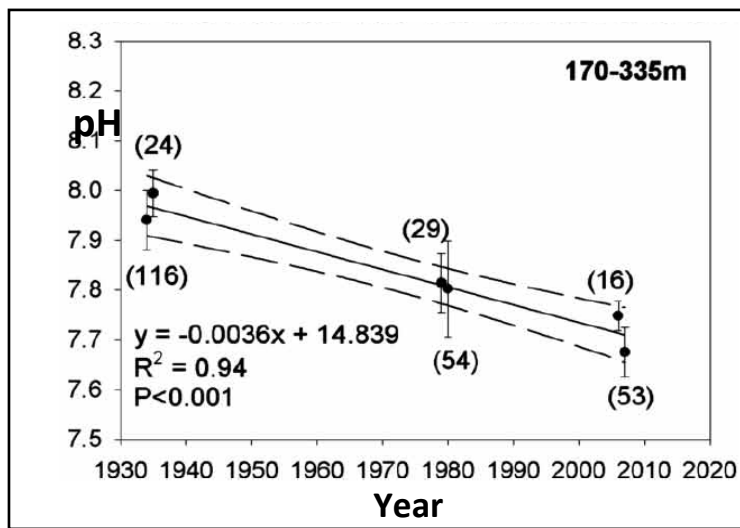
List of Tables

Table 1.1:	The chemical composition, reactivity, and surface area of various types of iron-oxyhydroxides commonly found in sediment. Sources: ⁱ (6), ⁱⁱ (7), ⁱⁱⁱ (5).	3
Table 1.2:	The chemical processes that occur in sediments, catalyzed by microorganisms that metabolize organic matter, using acetate as the model compound for the purpose of comparison. Modified from: Rickard, D. <i>Sulfidic Sediments and Sedimentary Rocks</i> , pp 390, (8).	7
Table 2.1:	The equations for the error functions used to evaluate the three isotherm models used in the study.	24
Table 3.1:	Isotherm parameters and values of the coefficient of determination (R ²) obtained through linear regression of the Langmuir and Freundlich models. Q _o : max. monolayer coverage (mg/g), n _F : adsorption intensity, K _L : Langmuir isotherm constant (dm ³ /mg), K _F : Freundlich isotherm constant (mg/g)	31
Tables 3.2 and 3.3:	Isotherm parameters and error functions values obtained for the Langmuir, Freundlich, and Redlich-Peterson (RP) models, computed using Microsoft Excel. The error functions are used to assess the compatibility of the fit of the model onto the experimental data. Q _o : max. monolayer coverage (mg/g), K _L : Langmuir isotherm constant (dm ³ /mg), n _F : adsorption intensity, K _F : Freundlich isotherm constant (mg/g), K _R : RP isotherm constant (L/g), α _R : RP isotherm constant (1/mg), g: RP isotherm exponent. The error functions are sum of squared deviation (SSD), chi-squared (χ^2), and the sum of absolute error (EABS).	34

1 1 Introduction

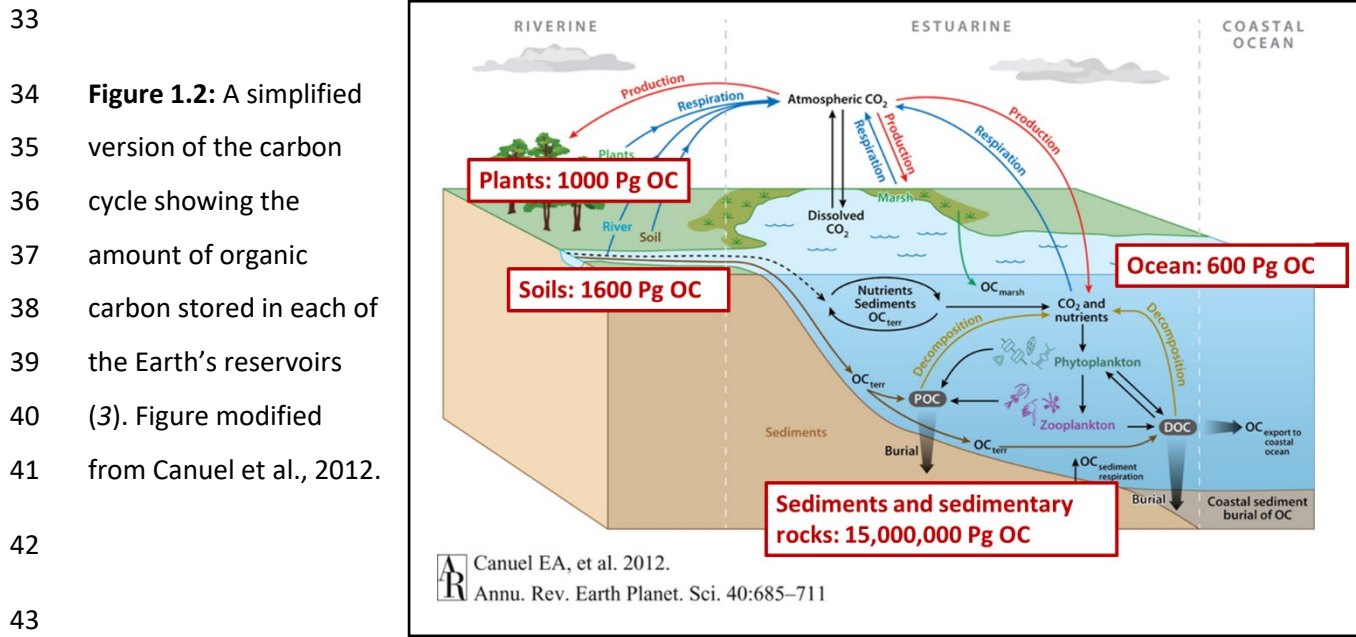
2 Perturbations in the global atmosphere and ocean systems due to human activity affect the elemental
3 cycles and in turn jeopardize life on this planet. In addition to decreasing biodiversity, climate change is
4 bound to rising atmospheric temperature and sea-levels, affecting an ever-growing number of people.
5 Among the various causes of climate change, the increased concentration of greenhouse gases, most
6 notably CO₂, have been held accountable for ocean acidification and increasing land and ocean
7 temperature. The ocean and other water systems act as buffers to climate change through absorbing
8 the added heat and CO₂, but the increasing concentration of CO₂ in the water column produces carbonic
9 acid (H₂CO₃), which decreases the pH of the system. Industrial activity is one of the most significant
10 sources of CO₂ on a global scale; from about year 1750 to 2019 the concentration of atmospheric CO₂
11 has risen from 280 to 411 ppm (9, 10). The ocean has partly balanced this increase in atmospheric CO₂
12 and thus incurred a decrease in pH, for example in the bottom waters of the St. Lawrence Estuary, from
13 1935 to 2007 the pH has dropped from 7.9-8.0 to 7.7 (Fig. 1.1) (2). The change of 0.2 pH units especially
14 affects organisms that biogenically produce CaCO₃, such as coral reefs and coccolithophores (11).

15 **Figure 1.1:** pH measurements
16 taken between year 1930 and 2010
17 from the Lower St. Lawrence
18 Estuary with a 95% confidence
19 interval. Samples were collected at
20 a depth between 170-335m. The
21 number in parenthesis represents
22 the number of data points. Figure
23 modified from Mucci et al., 2011.



24
25 Considering the ever-growing CO₂ concentration, it is essential that we understand how the various
26 Earth systems in place act as carbon sinks. Figure 1.2 shows the amount of carbon stored in each of the
27 Earth's reservoirs and demonstrates that sediments and sedimentary rocks hold a large proportion of
28 both organic and inorganic carbon (Fig 1.2). The pool of organic carbon (OC) is found in the form of
29 highly altered organic matter (OM) detritus from deceased fauna and plants and can originate from
30 terrestrial or marine sources. Left unprotected, the majority of the OM is remineralized to CO₂ by living

31 organisms (for example, as through bacterial respiration) and joins the global CO₂-pool as bicarbonate,
32 HCO₃⁻, to eventually become atmospheric CO₂.



44 Looking into the carbon cycle in marine systems, about 90% of OM is remineralized in the water column
45 before reaching the sediment-water interface (3, 12), and more than 90% of that OM is then
46 remineralized in the sediment following deposition (13). The remaining ~ 0.5% of OM is preserved or
47 “protected” in the sediment (3), and it is integral to understand the sediment chemistry influencing the
48 mechanisms behind this preservation for us to predict how the sedimentary carbon pool will react to
49 climate change, i.e. ocean warming and acidification.

50 **1.1 Sediment Chemistry and Composition**

51 The particles that make up sediment vary in size, from fine to coarse, and are often categorized based
52 on the specific particle sizes, or diameter(d), of each fraction; the most prevalent being clay (d=
53 <0.002mm), silt (d= 0.002mm-0.063mm), and sand (d= 0.04mm-4.75mm). Sediment can contain up to
54 90% pore water by volume (14), with the solid-phase consisting of silt/clay and sand. The amount of
55 particulate organic carbon (POC) in the sediment can vary from about 0.1 to 10 wt% (3). The most
56 geochemically relevant sedimentary minerals are clay fractions due to their small particle size, leading to
57 a higher reactivity with dissolved species through surface sorption, and higher relative abundance
58 (compared to the other fractions). Clays can contain various metals such as Al, Fe, Mn, Ni, Cr, and
59 several other minor elements, which can be present in the form of a Si-alloy, carbonate, or

60 (oxy)hydroxides, among other types of complexes. Specific elemental composition of sediment depends
61 on the source material from where the sediment originated, the current chemical environment (ie. pH,
62 redox potential (Eh), temperature), the rate and type of flux, and the extent of mixing (bioturbation) and
63 diagenesis.

64 Iron is supplied to the ocean in both dissolved and particulate forms. The major sources of iron to the
65 ocean are (from the highest flux to the least) fluvial inputs, sediments from melting glacial shelves,
66 atmospheric deposition, hydrothermal vent inputs, coastal erosion, and anthropogenic (resulting from
67 human activity) inputs (15, 16). Conventionally, dissolved material is classified as that which can pass
68 through a 0.2 to 0.7- μ m filter, and particulate is defined as that which cannot. Dissolved iron in the
69 ocean is found at a concentration of between 0.1 and 2.5 nM in the water column (8), a concentration
70 which challenges our analytical techniques, and approaches the minimum required for microorganism
71 survival. Coastal sediments typically contain around 3-5% of particulate iron by mass (17), which in
72 aerobic/oxic sediment are commonly found in the form of iron-(oxy)hydroxides and oxides (herein this
73 group will be referred to as iron oxides), found in various chemical formulas and reactivities. A
74 comparison of the various Fe oxides' chemical formulae, surface areas, reactivities to dissolved sulfide,
75 and standard energies of formation (ΔG_f^0) are shown in Table 1.1.

76

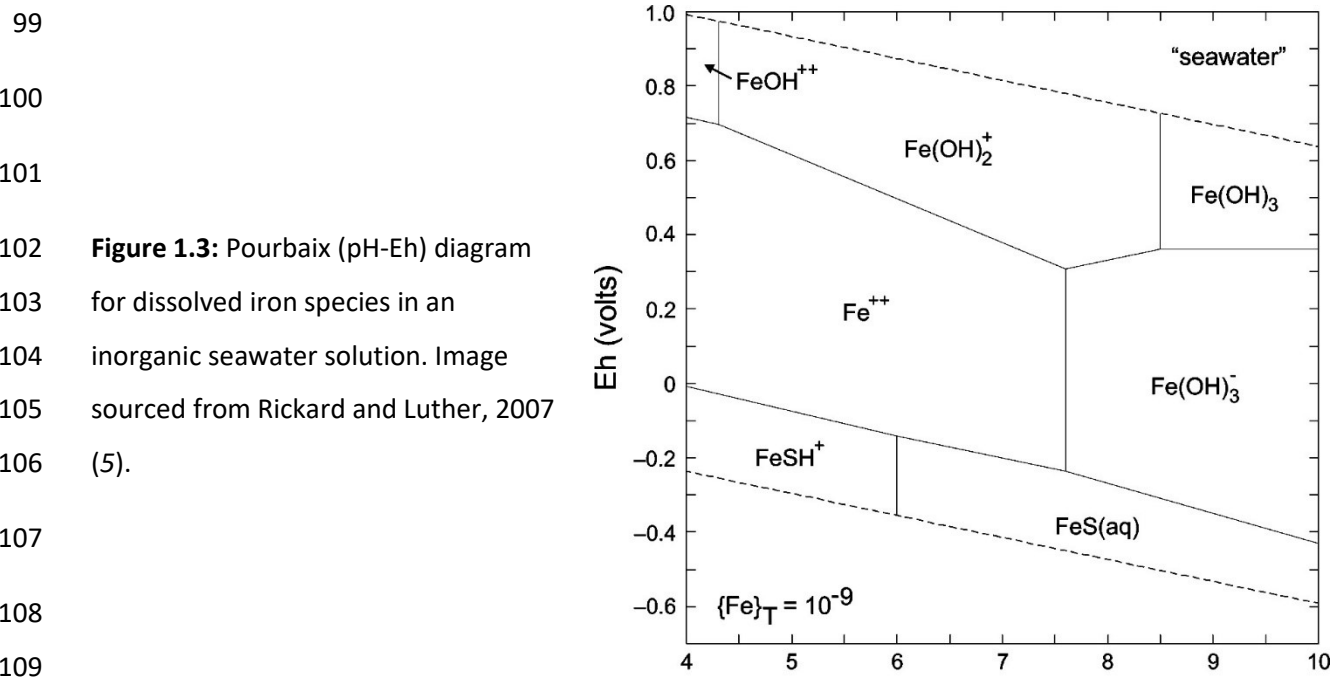
Species	Chemical Composition ⁱ	Surface area ^j (m ² g ⁻¹)	Reactivity ⁱⁱ (half lives for dissolved S ²⁻ concentration of 1000 μ M)	ΔG_f^0 ⁱⁱⁱ (kJ mol ⁻¹)
Ferrihydrite	Amorphous Fe(OH) ₃ or 5Fe ₂ O ₃ · 9H ₂ O	100-400	12.3 h	-708.5
Lepidocrocite	γ -FeO(OH)	15-260	10.9 h	-470.7
Goethite	α -FeOOH	8-200	63 days	-488.6
Hematite	α -Fe ₂ O ₃	2-90	182 days	-755.5
Magnetite	Fe ₃ O ₄	4-100	72 days	-1015.5

77 **Table 1.1:** The chemical composition, reactivity, and surface area of various types of iron-oxyhydroxides
78 commonly found in sediment. Sources: ⁱ(6), ⁱⁱ(7), ⁱⁱⁱ(5)

79

80 Ferrous iron in water is chemically stable as hexaaqua Fe(II), but ferric iron is not stable as a hydrated
81 ion species because of the greater charge on the nuclei, delocalizing electrons from the oxygen atom in
82 the water molecule in the hydration shell and eventually resulting in the formation of insoluble Fe(III)
83 hydroxides, and therefore exists in the dissolved phase as a Fe(III) hydroxyl complex, Fe(OH)₂⁺ (8). Figure

84 1.3 displays the Pourbaix diagram showing the dissolved iron species in seawater with dominant stability
 85 over the specified range of pH and Eh. This figure shows that at common seawater values ($Eh = 0.3$ V
 86 and $pH = \sim 8.2$) Fe^{2+} , $Fe(OH)_2^+$, and $Fe(OH)_3^-$ are almost of equal prominence, indicating that the dynamic
 87 nature of sediment pore water chemistry is sensitive to slight changes in the chemical environment. Iron
 88 oxides, including $Fe(OH)_2^+$, are not significantly soluble at seawater pH (18), and precipitate primarily as
 89 amorphous ferrihydrite, which eventually transforms into more stable iron oxides such as goethite or
 90 hematite. Iron oxides are found in a variety of structures and stabilities, resulting in a range of mineral
 91 phases that can be divided into “reactive” and “refractory” iron oxides. One major source of dissolved
 92 $Fe(II)$ in natural aquatic systems is from the reductive dissolution of iron oxides by microorganisms. Fe-
 93 reducing bacteria have been shown to favourably utilize the more reactive Fe oxide phases as their
 94 electron acceptor (19, 20), resulting in a longer lifetime of more refractory/crystalline phases. In the
 95 sediment solid-phase, iron oxides constitute a major proportion of solid-phase Fe but other Fe -
 96 containing species such as siderite ($FeCO_3$) and pyrite (FeS_2) also contribute. In sediment pore water
 97 $Fe(II)$ dominates, and though $Fe(III)$ has limited solubility in the dissolved phase, solubility is increased by
 98 about 25% when complexed to organic ligands (21, 22).



111 The sedimentary system of solid to dissolved Fe (and vice-versa) in sediments is not an isolated one;
 112 other ionic species, microorganisms, as well as organic matter (OM) are abundant in the water column
 113 and pore water. Interactions between dissolved iron and dissolved organic matter (DOM) have been

well recorded in geochemistry (as well as biochemistry), largely due to the strong binding and affinity between the two species. Siderophores are organic molecules secreted by microorganisms to bind Fe in solution, often through chelation of Fe(III) through multiple binding sites containing functional groups such as catechol, hydroxamic acids, and α -hydroxy carboxylic acids (23). Siderophores are known for promoting extremely stable complexes with Fe(III) due to a few factors: for example the increase of entropy from replacing the water atoms around Fe(III), and the kinetic stability through the strong ionic interactions between the metal and ligand (24). Ligands which contain oxygen as the donor atom can act as a hard Lewis base which react favorably with hard Lewis acids such as Fe^{3+} due to the similarity in energy of the frontier orbitals; the high energy highest occupied molecular orbital (HOMO) of oxygen and the high energy lowest unoccupied molecular orbital (LUMO) of Fe^{3+} (25). The purpose of siderophore release is to keep the Fe soluble, for later uptake into cells (23). Siderophores are mostly known for binding Fe(III), as Fe(II) is a soluble species under anoxic conditions and can be transported into cells without assistance from a siderophore. Often the release of Fe(III) from the siderophore is initiated by the reduction into Fe(II), for which the siderophore does not have significant affinity (24). Despite the strength of siderophore-Fe complexes, there are other organic molecules that interact with Fe(III) in marine systems, such as that from OM originating from plant and animal debris, and from microorganisms.

The binding stability of organic molecules with Fe(III) or Fe(II) in solution can be quantified through a stability constant (K), and although the molecular composition and structure of natural organic matter (NOM) are difficult to elucidate (26), this limitation can be overcome by using model compounds in controlled experiments. Stability constants are conditional on the experimental conditions, for example the pH or ionic strength, and represent the position of the equilibrium between the independent species and the complex. Large values of K represent a stable complex, and lower values represent complexes of lower stability. In the water column and in sediment pore water the most common types of biomolecules (besides siderophores) are the degradation products of phytoplankton or terrestrial detritus. Stability constants of Fe(III)-siderophore complexes range from around 10^{25} to 10^{50} (27), while stability constants for Fe(III)-NOM complexes have been reported to be around 10^{12} (28) and 10^{21} (22). Despite the limitations of comparing conditional stability constants, these values show that although it is hard for NOM to compete with siderophores for Fe(III), there are significant interactions between NOM and Fe(III). These interactions influence much more than Fe(III) solubility, they also influence the reactivity of Fe towards other species in solution, the rate at which Fe precipitates into the solid-phase, and the further transformation of OM.

146 **1.2 Chemical Cycles of C, O, Fe, and S in Sediment**

147 There is a global equilibrium in the continuous cycling of elements between the solid-phase in sediments
148 and the pore water, between the sediment-water interface and the water column, and between the
149 water column and the atmosphere. Arguably the most important elements in this cycle, due to their
150 biological importance and far-reaching associations to other elements, are carbon, oxygen, nitrogen,
151 iron, and sulfur. Except for iron for which gaseous species are not stable under natural conditions, these
152 cycles interact in all three phases, forming species that are sensitive to environmental conditions. The
153 carbon cycle is central to our biology and global climate and includes both inorganic and organic species.
154 In the atmosphere, carbon exists as CO₂ and CH₄, which make up 0.04% and 0.0002% of the atmosphere
155 by mole fraction, respectively, as well as in a broad range of volatile organic compounds. CO₂ is removed
156 from the atmosphere through photosynthesis or through the solubility equilibrium between the
157 atmosphere and ocean, in which case it will consequently become dissolved CO₂, then carbonic acid
158 (H₂CO₃) through reaction with H₂O, and then exists as bicarbonate and carbonate ions. Besides acting as
159 a buffer in aquatic systems, carbonates make up many shells and sedimentary rocks in ocean and
160 freshwater systems, and their dissolution (initiated by environmental conditions such as pH changes),
161 releases dissolved inorganic carbon (DIC) into the water. DIC and dissolved organic carbon (DOC) have a
162 relationship that is not estranged; DIC is also a product of respiration: microorganisms such as
163 sedimentary bacteria use DOC and/or particulate organic matter (POC) as their food source, degrading
164 DOM and producing CO₂ as a result. DIC can be removed from the water-atmosphere equilibrium
165 through the formation of shells by microorganisms such as coccolithophores. Inputs of OC to deep water
166 and sediment increase the O₂ demand of the environment through the metabolism (respiration) of
167 microorganisms.

168 Like carbon, oxygen also exists in equilibrium with the atmosphere and ocean. Dissolved oxygen is found
169 in a range of concentrations, from 0 to as much as 10 mg/L in surface waters, and penetrates sediment
170 from the sediment-water interface to depths that vary depending on the bottom water dissolved O₂
171 concentration, as well as sediment composition and microbial demand (29). This results in zones of
172 oxygen concentration that are labelled as suboxic (0.1 to 1.0 mg/L) and anoxic (<0.5 mg/L to below the
173 detection limits of our analytical instruments) (30). Sediment which is depleted in O₂ is also labelled as
174 hypoxic (O₂-limited), and it is caused by restricted water circulation, a lower rate of O₂ diffusion into the
175 sediment and consumption in situ by microbial activity and reaction with reduced inorganic species (31).
176 The Eh in a specific sediment is influenced by the concentration of dissolved O₂ which influences the

177 speciation of redox sensitive elements like Fe, Mn, S, and several other minor elements. Oxygen acts as
178 an electron acceptor for microbial activity, gaining energy from the following reaction, using C₆H₁₂O₆,
179 glucose, as a model compound:



181 This reaction has a ΔG° of -2870 kJ per mole of glucose (32) and produces DIC. As oxygen in the bottom
182 waters can be limiting, the available O₂ for microbial activity decreases with depth in the sediment
183 profile. Other chemical species fulfill this role, in an order that follows the amount of energy that is
184 released, Table 1.2 shows the ΔG_r° for the reactions down-core using acetate as the electron donor in
185 OM. Figure 1.4 shows the typical trends in relative abundance of electron acceptors for microbial
186 activity in the pore water below the sediment-water interface, corresponding in trend to the amount of
187 free energy released by the reaction.

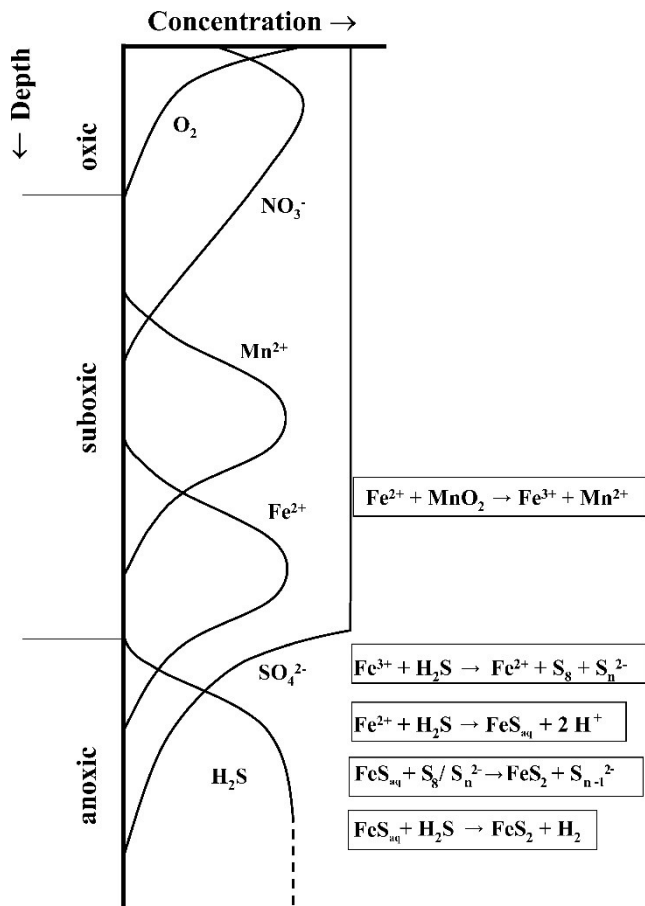
Process	Chemical Equation	ΔG _r ° (kJ/electron)
Aerobic respiration	$O_2 + 0.5CH_3COO^- \rightarrow HCO_3^- + 0.5H^+$	-101
Denitrification	$NO_3^- + 0.125H^+ + 0.625CH_3COO^- \rightarrow 0.5N_2 + 1.25HCO_3^- + 0.5H_2O$	-90
Mn(IV) reduction	$MnO_2 + 1.75H^+ + 0.25CH_3COO^- \rightarrow Mn^{2+} + 0.5HCO_3^- + H_2O$	-97
Fe(III) reduction	$FeOOH + 1.875H^+ + 0.125CH_3COO^- \rightarrow Fe^{2+} + 0.25HCO_3^- + 1.5H_2O$	-60
Sulfate reduction	$SO_4^{2-} + H^+ + CH_3COO^- \rightarrow H_2S + 2HCO_3^-$	-11
Methanogenesis	$CH_3COO^- + H_2O \rightarrow CH_4 + HCO_3^-$	-5

188 **Table 1.2:** The chemical processes that occur in sediments, catalyzed by microorganisms that metabolize
189 organic matter, using acetate as the model compound for the purpose of comparison. Modified from:
190 Rickard, D. *Sulfidic Sediments and Sedimentary Rocks*, pp 390, (8).

191 After the depletion of oxygen in the sediment profile (leading to suboxic and anoxic zones), the next
192 electron acceptor is nitrate, which is transformed into nitrite, gaseous nitrogen, or ammonium (33).
193 Following the use of nitrate by microorganisms is the use of manganese. Mn is present in the solid-
194 phase largely as Mn(IV/III)-(hydr)oxides such as MnO₂ and MnOOH (34), which, like Fe, exist in a range of
195 structures and undergo reductive dissolution by microbes or by dissolved sulfide, forming Mn(H₂O)₆²⁺
196 and Mn³⁺-OM complexes in the dissolved phase (35). The chemical equations for reductive dissolution of
197 solid-phase Fe and Mn by dissolved sulfide in sediments is proposed as follows (36):

198	$2\text{FeOOH} + 3\text{H}_2\text{S} \rightarrow \text{S}^0 + 2\text{FeS} + 4\text{H}_2\text{O}$	$\Delta G^0 = -79 \text{ kJ/mol}$	$\Delta G_r = -57 \text{ kJ/mol}$
199	$\text{MnO}_2 + \text{HS}^- + 3\text{H}^+ \rightarrow \text{Mn}^{2+} + \text{S}^0 + 2\text{H}_2\text{O}$	$\Delta G^0 = -52 \text{ kJ/mol}$	$\Delta G_r = 34 \text{ kJ/mol}$

200 ΔG^0 is the standard-state free energy and ΔG_r is the free energy at in-situ conditions. Accumulation of
 201 Mn in the pore water can be an indicator of microbial activity, but only if the rate of reductive
 202 dissolution is greater than that of Mn migration into oxic zones, where it is re-oxidized. As shown in
 203 Figure 1.4, Mn(IV) can also be reductively dissolved by other reduced species like Fe^{2+} , which commonly
 204 is produced by Fe(III)-oxide reduction at depths deeper into the sediment. Ferric iron- and sulfate-
 205 reducing prokaryotes are ubiquitous in sediments globally and are responsible for producing most (37)
 206 of the Fe^{2+} and $\Sigma\text{H}_2\text{S}$ ($\Sigma\text{H}_2\text{S} = \text{H}_2\text{S} + \text{HS}^- + \text{S}^{2-}$) in sediments. Despite the high pK_2 of H_2S (estimated at >18)
 207 leading many to believe that S^{2-} does not have significant activity at seawater pH, its activity is relevant
 208 to solubility equilibria of metal-sulfide species (5). Reductive dissolution of Fe-oxides release Fe^{2+} which
 209 can remain dissolved in the pore water, migrate upwards to be oxidized as it reduces another species, or
 210 precipitate as an iron sulfide using the dissolved H_2S in solution. Mackinawite (FeS) is typically the first
 211 iron sulfide precipitated out of the pore water when Fe^{2+} and $\Sigma\text{H}_2\text{S}$ are present. Mackinawite is a
 212 metastable compound by function of its sensitivity to oxidation by O_2 , and has been shown to transform



into greigite (Fe_3S_4), elemental sulfur (S^0), or iron hydroxides over a period of hours (38). The fate of FeS ultimately depends on the oxygen concentration in the sediment, which controls the redox boundaries and in turn the speciation of many metals and minerals.

Figure 1.4: A simplified representation of the relative abundance of dissolved redox-active species in the sediment profile, from the sediment-water interface to depth. Image sourced from Rickard and Luther, 2007 (5).

228 Most animal life cannot survive in hypoxic conditions which are often described as having an $[O_2] < 2$
229 mg/L (39). Sediments can be exposed to periods of oxidation followed by periods of anoxia. One
230 convention in place to describe the history of sediment with respect to oxygen is by the “oxygen
231 exposure time” (OET). As OET changes in a sediment there are implications not only for the chemical
232 speciation but for the fate of OM; re-exposure to O_2 after being in an anoxic environment increases the
233 degradation of OM. The effect of OET on the rate of OM degradation depends on the nature of OM (40).
234 OM can be divided into two fractions: labile (recently deposited, fresh phytoplankton, amino acids, and
235 sugars) and refractory (polymers such as lignin, photosynthetic pigments; OM which is hydrolysis-
236 resistant) (3). Anoxic and mixed-redox sediment shows different types of OM, and revealed by
237 fluorescence; anoxic sediments show higher concentration of humic-like substances (41). Several studies
238 have shown that fresh labile OM is degraded at similar rates irrelevant of OET while more refractory OM
239 is degraded significantly faster with O_2 compared to without (40–42). Typically, in sediment pore water a
240 majority of the DOC falls into the refractory portion with the maximum concentration of labile OM at
241 the sediment-water interface (41). Some of this DOC (the labile fraction included) is also preserved
242 through interactions with minerals in the solid-phase of the sediment through sorptive interactions,
243 which may be preventing the degradation of OM and in turn the release of CO_2 to the atmosphere.

244 **1.3 Carbon Preservation by Iron Oxides in Sediment**

245 Burial of OC in sediments is thought to be responsible for preserving up to 0.5% of OC that enters the
246 water column (3), and while this may seem like a modest portion, it is significant because of the
247 abundance of sediment on Earth: sediment covers about 70% of the Earth’s surface (43). There are four
248 main mechanisms that have been proposed for OM preservation in sediment: OM is resistant to
249 degradation due to the environmental conditions or its molecular make-up, OM is protected within
250 biogenic minerals, OM is protected through aggregation with minerals, and OM is protected through
251 sorption onto mineral surfaces (44). The hypothesis of the responsibility of iron oxides in OC sorptive
252 preservation began by observations of a correlation between the amount of fine-grained material (clay
253 minerals) in the sediments and soil and the concentration of OC (3, 45). Mayer and coworkers
254 hypothesized that the correlation between sediment grain size and OC concentration was because of
255 sorptive type interactions between OM and the minerals (46, 47). It has since been found that up to 70%
256 of OC in sediment is associated with mineral grains (44). There are a significant number of minerals in
257 clay and soils that are known to have a sorptive interaction with OC, for example Al and Fe oxides. In the

258 past 20 years, the role of Fe oxides specifically in stabilizing OC in sediments and soils has been
259 thoroughly explored and its importance defined (48).

260 The prominence of iron in Earth's geochemical cycles and numerous roles in biological systems is due to
261 its ability to form stable complexes, owing to the extremely stable ^{56}Fe nucleus (49). Fe(II) and Fe(III) are
262 d^6 and d^5 cations, respectively, and this results in distinct chemical behaviour between the two oxidation
263 states. According to Pearson's Hard Soft Acid Base (HSAB) theory (25), Fe(III) is a hard acid which forms
264 the strongest complexes with hard bases such as O, N, and F. Fe(III) can also form complexes using O or
265 OH as a bridge. Fe(II) is between a hard and soft acid, and forms stable complexes with soft bases (such
266 as S) but can also be stabilized by hard bases like organic ligands. The ligands (organic and inorganic)
267 present in aqueous solution with the iron cations influence the ligand field stabilization energies (LFSE)
268 of their HOMO and LUMO. Both cations form complexes in high- and low-spin octahedral states
269 depending on the ligands available. A higher LFSE denotes a more stable complex. Ferrous iron has been
270 most commonly observed in the high-spin configuration because of the ligands available in natural
271 systems, for example H_2O which is a medium-field ligand (50). In the water column, two classes of Fe-
272 binding ligands have been observed; strong binding ligands at shallow depths and weaker binding
273 ligands at depth (51).

274 The oxidation state of iron in the water column and sediment pore water may be controlled by the
275 organic ligands present, which are influenced by the environmental pH and Eh (49) but are also affected
276 by the presence of O_2 and NO_3^- , which can act as oxidants (52). Ferrous iron may be stabilized even in
277 oxygenated water through the complexation by organic ligands, and indeed Fe(II) has been observed to
278 be present in significant concentrations (relative to Fe(III)) in well oxygenated waters as an OM-bound
279 species (53). The half-life of dissolved Fe(II) towards oxidation has been measured to be on the order of
280 minutes (49) but on the order of days when in the presence of or bound to NOM (54, 55). The reduction
281 of Fe(III) to Fe(II) in natural systems is largely caused by photoreduction in the surface waters, by
282 dissimilatory iron reduction (reduction of Fe(III) by anaerobic bacteria), and by reaction with other
283 chemical species such as sulfide which can reduce the less crystalline forms of Fe-oxide (7).

284 The abundance of Fe oxides in lake and marine sediments is around 20-60% of the total solid-phase Fe
285 (48, 56, 57). In these natural environments Fe oxides inevitably interact with species present in the
286 sediment matrix such as DOM, which has been shown to have an inhibitory effect on Fe oxide
287 crystallization (58), for example, the transformation of ferrihydrite into more stable forms of Fe oxide
288 such as lepidocrocite or goethite (59, 60). NOM can interfere with Fe oxide formation in the following

289 ways: by sorption onto the surface (preventing growth), binding to Fe in solution (inhibiting
290 precipitation), or even increasing growth through acting as a template (61). The presence of Fe-oxide
291 aggregates containing DOM was confirmed in 1971 by Akiyama (62); these aggregates are commonly
292 referred to as co-precipitates (formed through co-precipitation), whereas particles with DOM found on
293 the surface are formed by adsorption. The affinity between OM and Fe oxide is partly governed by
294 outer-sphere electrostatic interactions that are dependent on the pH of the system; sorption increases
295 with decreasing pH because the Fe oxide surface becomes more positively charged, a trend that
296 increases until the ligand is positively charged as well (63). Besides electrostatic interactions, a ligand-
297 exchange reaction could be occurring between the positively charged (at marine pH) hydrated Iron(III)
298 hydroxides and the negatively charged OM in colloidal and dissolved form (64), forming inner-sphere
299 covalent interactions both through aggregation (co-precipitation) and superficial adsorption, as shown
300 using XANES analysis (48). An inner-sphere interaction as the dominant mechanism has also been found
301 using model compounds such as lactate (65) and NOM containing hydrophobic and hydrophilic moieties
302 (66).

303 An increase in pH as OM is sorbed onto the Fe oxide mineral is an indicator that NOM may be
304 substituting -OH groups on the Fe oxide surface (66), and revealing which C-functional groups of the OM
305 that are involved have been the goal of several studies using both model compounds and NOM. In soil, it
306 has been found that hydrophobic OM is preferentially sorbed to minerals relative to hydrophilic OM
307 (67), and that a gain of entropy may be driving the sorption (68). Humic and fulvic acids are widely used
308 in studies as a NOM source modelling pedogenic OM: older material of a high molecular weight (>3000
309 Da) originating from terrestrial sources. DOM from terrestrial origin contains mostly intermediates of
310 lignin and cellulose decomposition and it has large proportions of carboxyl and hydroxyl groups (66). OM
311 originating from a terrestrial source may sorb onto Fe oxides with higher strength than OM from a
312 marine source due to the lower proportion of labile OM, which is found in aquagenic origin (fresh OM,
313 smaller molecules including polysaccharides) (53). High molecular weight NOM may be better at
314 stabilizing colloids of NOM-Fe oxides because the polymer chain promotes stabilization (66). Besides
315 carboxyl and hydroxyl, Fe oxides have been shown to preferentially sorb other functional groups in
316 DOM: aromatics, amino acid residues, and carboxylic acid (69), O-alkyl (attributed to carbohydrates)
317 (60), and phenolic hydroxyl groups (64). The binding of the OC moiety to the Fe oxide mineral is
318 hypothesized to occur through irreversible reactions with the mineral surface (70) and this has
319 implications for sedimentary carbon storage.

320 **1.4 Sulfidation of Iron Oxides and the Precipitation of Iron Sulfides in Sediment**

321 Adsorption and co-precipitation of DOM onto Fe oxides is a mechanism that protects and preserves OC
322 from being degraded; as observed for soil OM, desorption is required for microbial use of the OM (71).
323 One study found that unless DOM in river water is sorbed to minerals, it is quickly degraded by oxic
324 biodegradation or photolysis (67). Despite protecting the DOM from degradation, the interaction
325 between DOM and Fe oxides poisons the Fe oxide mineral structure, lowering the Fe oxide crystallinity
326 therefore increasing the reactivity of Fe oxides formed (59). Indeed, the bioavailability of Fe is governed
327 by the Fe oxide crystallinity (72) and in sediment, Fe oxides that are considered highly reactive towards
328 dissolved sulfide have been found to be intimately associated to OC (73). Reductive dissolution of Fe
329 oxides can occur in natural anoxic environments in a variety of ways: respiration by Fe-reducing
330 bacteria, coupled to the oxidation of OM by heterotrophic bacteria, and by reduction by hydrogen
331 sulfide produced by sulfate reduction (74). Sulfide is the most prominent abiotic reductant for Fe(III)
332 (75), but its reactivity toward Fe oxides depends on the surface properties and crystallinity of the Fe
333 oxide nanoparticles: ferrihydrite reacts faster than hematite, which reacts faster than goethite (74). This
334 reaction results in the sulfidation of Fe oxides in anoxic sediment typically producing metastable iron
335 sulfide (FeS), which can persist over long periods of time given favourable environmental conditions
336 such as low reduction potentials.

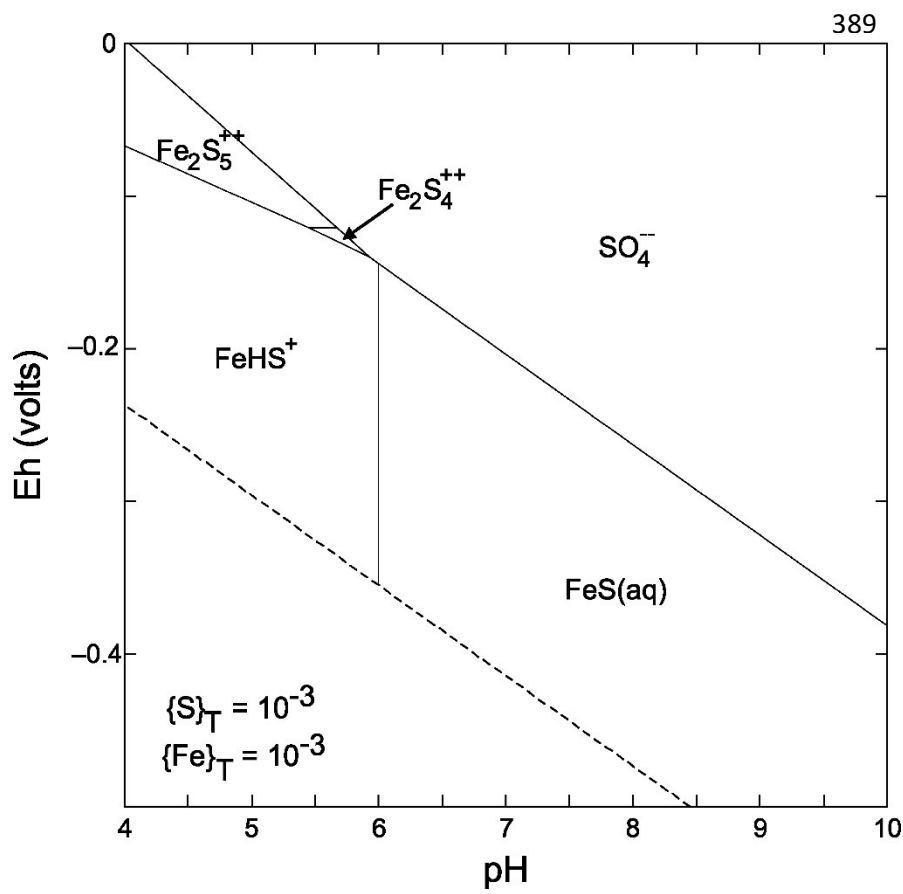
337 The reduction potential is a significant parameter used to describe the conditions in a specific
338 sedimentary environment. The redox boundary in a sediment profile describes the location of the
339 transition from oxidative to reductive conditions and it is not fixed; it varies spatially depending on
340 temperature, O₂ concentration in bottom waters, bacterial activity, and inputs of OM. Climate change
341 may influence the redox boundary through the dissolved O₂ concentration, which is dependant on
342 temperature, limited by O₂ supply and microbial activity (76). The sediment can be described as
343 reducing, oxidizing, or mixed-redox, the latter representing sediments subjected to periods of varying
344 reduction potential (reduction and oxidation cycles, most often in high energy systems that undergo
345 abrupt current or wind driven resuspension and deposition cycles). Model simulations have shown that
346 the redox boundary in sediments that are organic-poor are sensitive to inputs of OM, causing the redox
347 boundary to move to a shallower depth (76), and exposing previously stable complexes (such as Fe
348 oxides) to reducing conditions. In these conditions, reducing species such as sulfide are present, which
349 can reduce Fe oxides. In aquatic environments, the thermodynamically stable chemical species of sulfur
350 are hydrogen sulfide, elemental sulfur, and sulfate (77). Sulfide is mostly produced from the biologically-

351 mediated reduction of sulfate. The abiotic reduction of sulfate in the environmental conditions found in
352 marine sediments is extremely slow, due to the stability of the short SO_4^{2-} sulfur-oxygen bonds.
353 Microorganisms can overcome the bond stability using large enzymes that elongate the S-O bond,
354 facilitating the reduction of the sulfur atom, a reaction which has a Gibbs energy change of -232 kJ/mol
355 (8).

356 Sulfide in solution exists as either H_2S , HS^- , or S^{2-} , depending on the pH of the system. The $\text{pK}_{1,\text{H}_2\text{S}}$ is about
357 7 (78), therefore at a pH relevant to sediment (~8.2) most of the sulfide is present as HS^- . Due to the
358 positions of the HOMO and LUMO for H_2S and HS^- (the HOMO of H_2S is more stable), HS^- is the better
359 nucleophile (8). Other sulfidic species present in water in less prominent concentrations include
360 polysulfides, sulfur oxyanions, and sulfur free radicals. The products of sulfide oxidation that are soluble
361 include thiosulfate and sulfite, elemental sulfur, and organic sulfides (77). Sulfide oxidation in sediments
362 is not only coupled to the reduction of molecular oxygen through microbial activity, but it is also coupled
363 to the reduction of Mn(III)/(IV) and Fe(III) (79). The mechanism of reductive dissolution of Fe(III) oxides
364 by HS^- has been suggested to proceed through a reaction scheme beginning with the surface sorption of
365 hydrogen sulfide. Briefly, initiated by an inner-sphere surface complexation, an electron is transferred
366 from the sulfur atom to Fe, producing Fe(II) and a sulfur radical, followed by the release of the sulfur
367 radical, which then reacts with the Fe(III) oxide surface to produce S^0 and free Fe^{2+} (80). In this way, the
368 surface of the Fe oxide is gradually reductively dissolved, as long as there is an abundance of sulfide ions
369 in solution. The rate of reductive dissolution of Fe oxides by sulfide was measured to be a direct function
370 of the surface reactivity, which is a condition of the Fe oxide's formation (81).

371 The fate of the released Fe^{2+} immediately after reductive dissolution is dependent on the chemical
372 species present, but in aqueous solutions it will be first present after reductive dissolution of Fe(III) as a
373 hexahydrate, $[\text{Fe}(\text{H}_2\text{O})_6]^{2+}$. The reaction of aqueous Fe(II) with dissolved bisulfide (HS^-) has been
374 experimentally determined to follow an Eigen-Wilkins scheme (82) where the association of bisulfide to
375 the complex occurs through nucleophilic substitution forming $\text{Fe}(\text{HS}) \cdot (\text{H}_2\text{O})_5^+$. The release of the inner-
376 sphere water molecules is thought to be the rate-limiting step (83), driven by an increase in entropy
377 (84), which results in a change of the coordination around the Fe(II) atom. The resulting $[\text{FeSH}]^+$ complex
378 loses a proton in conditions found in marine environments (Figure 1.5), and as a result is considered an
379 intermediate to the formation of aqueous iron-sulfide clusters (FeS_{aq}) (85). FeS_{aq} has been observed in
380 the water column of lakes (86) and marine environments (87) as well as in the pore water of estuarine
381 and marine sediments (88). The solubility of FeS_{aq} reaches saturation at $10^{-5.7}$ M (89), at which point it

382 precipitates as mackinawite, FeS_m . Precipitation of FeS_m has been shown to occur on the order of
 383 milliseconds to seconds (84) and is identified in sediments by its black-grey colour. Though mackinawite
 384 has been labelled as “metastable” (relative to pyrite, FeS_2), it has been observed to be stable in
 385 sediment on the order of 10^3 yr, provided H_2S is not present in significant concentration (90). The
 386 prominence of FeS_m in sediments varies depending on the pH, Eh, and concentrations of Fe^{2+} and sulfide
 387 in the system. The concentration of sulfide in the pore water is controlled by sulfate reduction which is
 388 controlled by OM availability (74), which may be particularly relevant in estuarine and lacustrine systems



389 where the input of OM is
 highest (91, 92).

Figure 1.5: Pourbaix diagram showing the speciation of dissolved iron-monosulfide at activities of iron and sulfur that approach those found in natural systems. In marine conditions, aqueous mackinawite is expected to exist at FeS_{aq} . Image sourced from Rickard and Luther, 2007 (5).

406 1.5 Iron Monosulfide (“Mackinawite”) and Organic Matter

407 Aqueous iron-sulfide clusters have prominent importance in biochemistry; they are found in several
 408 proteins as the centre which can facilitate redox reactions through gaining and loosing an electron. One
 409 such protein is ferredoxin, which contain thiols bound to Fe-S clusters; Fe-S is coordinated to cysteine
 410 (93). In sediments, dissimilatory sulfate reduction interacts with the carbon cycle through the
 411 mineralization of carbon, which influences the rates of organic matter preservation in sediments. Sulfate
 412 concentration is inversely correlated to DOC concentration, suggesting that the supply of this electron

413 donor is what controls sulfate reduction (94). The sulfur and carbon cycles also interact through OM
414 containing S-moieties, which can originate from terrestrial or marine sources. Sulfur in OM is bound
415 largely to O, such as ester-sulfates ($R-O-SO_3H$), and carbon functional groups ($R-SH$), mostly originating
416 from amino acids. Hydrolysis (mineralization by microorganisms) of the ester-sulfates is expected to
417 produce sulfate, and the hydrolysis of the $R-SH$ groups produces sulfide (36). OM can also undergo
418 sulfidization in anoxic sediment by hydrogen sulfide (92), which can prevent or hinder microbial
419 degradation, acting as a mechanism to preserve OM (95). In anoxic sediment pore water, FeS_{aq} is
420 typically saturated, leading to the precipitation of disordered FeS, that over time transforms into more
421 stable phases like ordered FeS_m if under reduced conditions, or greigite and pyrite if not (96).

422 It has been confirmed using X-ray powder diffraction (XRPD) that the first phase of synthetic FeS that
423 precipitates in laboratory experiments is considered to be “disordered” because it precipitates
424 stochastically as amorphous particles that only become more crystalline over time (97, 98). FeS can be
425 precipitated using Na_2S or $NaHS$, or by using live sulfate-reducing bacteria (SRB) as the sulfide source.
426 The character of synthetic FeS is sensitive to the experimental methods of preparation such as other
427 components in the system and aging time (96), but nonetheless, the surface chemistry and aggregation
428 characteristics have been explored. Synthetic FeS_m is found in a “platy” form; its structure is that of
429 layers, containing Fe-Fe bond distances within the sheets of 2.5967 Å (99), about half as long as the Fe-
430 Fe distances in ferrihydrite and hematite (100). Several studies have found that the surface of FeS_m is
431 dominated by sulfide groups (96). The zero point charge (pH_{ZPC}) of disordered FeS is at around pH 7.5,
432 above pH 7.5 the surface becomes negatively charged, and lower than pH 7.5 the surface become
433 positively charged, until it reaches saturation at pH ~6.5 (96). In a review on iron sulfide chemistry,
434 Rickard and Luther (2007) asserted that FeS_m in natural systems will be associated to a counter-ion,
435 which may be an organic ligand (5). The nature of this possibility has not been thoroughly explored, but
436 several studies have touched on the subject of FeS-OM interactions, as detailed below.

437 In sediment pore water there exists many species such as metal ions and organic molecules that are
438 known to have an impact on the iron-sulfide system in terms of transformations between the dissolved
439 and solid-phase, and the oxidized and reduced species. Greigite (Fe_3S_4) and pyrite (FeS_2) are the final end
440 stages of iron sulfides after two pathways of FeS oxidation (94). The transformation of FeS_m to Fe_3S_4
441 involves the partial oxidation of Fe through a solid-state reaction (101), and to form pyrite, FeS must
442 dissolve for the reaction to occur between the released products of dissolution (102). One study found
443 that the presence of organics had an effect on the Fe-S system at temperatures above 40°C; aldehydes

444 specifically were found to decrease pyrite formation (by decreasing dissolution) in favour of greigite
445 (101). Indeed, organics have been shown to prevent the oxidation of Fe(II) in hydrothermal vents,
446 possibly through sorption or complexation (103). Sorption has certainly been shown for iron sulfides
447 such as FeS, but the research has largely been in the direction of metal sorption. For example, FeS has
448 been shown to be an effective sorbent of arsenic (104), mercury (105), and selenium (106). A gap in
449 knowledge is evident when it comes to organic matter and FeS. The studies most pertinent to this work
450 have been done by Picard and colleagues looking at FeS-OM interactions from a biology perspective;
451 specifically considering the role of microorganisms in FeS formation (107–109). In these studies, Picard
452 finds that the presence of sulfate-reducing bacteria affects the precipitation characteristics of FeS. The
453 study presented in this thesis attempts to uncover more about this relationship; whether there is in fact
454 sorption between OM and FeS, whether NOM influences the aggregation of FeS, and if OM can protect
455 FeS from oxidation by atmospheric O₂.

456 **1.6 Objective and Arrangement of Thesis**

457 As described in the prior sections, the role of iron oxides in preserving OM in sediments has received
458 much attention. In comparison, the fate of this OM in sediment in a sulfidic/reducing environment has
459 not. The aim of this thesis is to explore this area by taking several different routes, each investigating a
460 unique characteristic of the FeS-OM interaction. The methods used in this study are explained in
461 Chapter 2. Sediment and pore water from sampling missions in 2017 and 2018 at stations SAG-05 and
462 STN-23 (which have sulfidic sediment at depth) was used for chemical analyses as well as scanning
463 transmission X-ray microscopy looking at the near edge X-ray fine structure (STXM/NEXAFS).
464 STXM/NEXAFS was used to find co-localization between Fe(II) (from FeS), Fe(III) (from Fe oxides) and OC
465 (from organic matter) in the natural sediment samples and synthetic FeS. Sorption isotherms were used
466 to identify whether DOM from natural sources has any interaction with already precipitated FeS in
467 terms of surface sorption, or if it interacts with FeS as it is precipitating (co-precipitation). The effect of
468 NOM's presence while FeS precipitated on the size and surface texture of the aggregates was examined
469 using scanning electron microscopy (SEM). Finally, a method used to dissolve reactive iron oxides will be
470 used to look at the effect of OM on the oxidation of FeS. The combination of these techniques and the
471 results that they will provide will increase our knowledge of how organic carbon interacts in these
472 anoxic systems.

473 Chapter 1 of this thesis details the background of sedimentary carbon, sulfur, iron, and oxygen cycles,
474 summarizes the character of FeS, as well as reviews the pertinent literature relating to this research. The

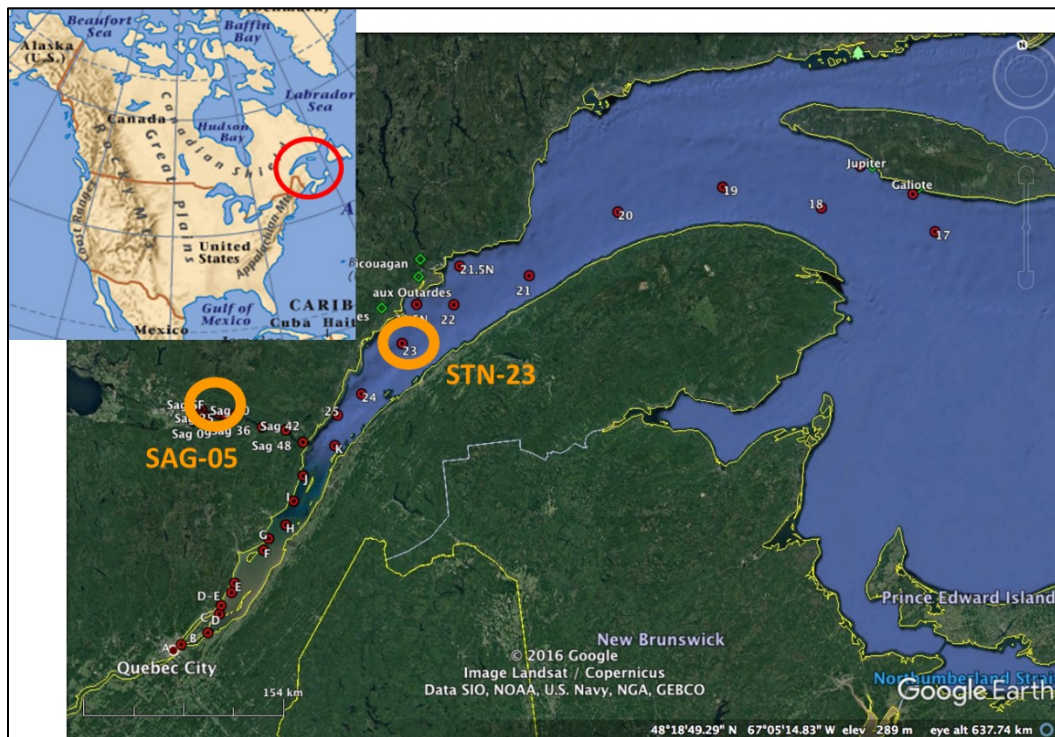
475 specific chemical analysis and techniques used are on the sediment samples and for the synthetic
476 precipitations are detailed in Chapter 2, which also explains the theory behind the isotherm models
477 applied to this data. Chapter 3 outlines the results of the field analyses and laboratory experiments and
478 contains the figures which have culminated. A discussion of our results in the context of past and
479 current research and the limitations of these results is included in Chapter 4. The thesis is concluded in
480 Chapter 5 which summarizes the implications of this study in light of previous research and indicates
481 future directions for research in this area.

482 **2 Materials and Methods**

483 All glassware used in this study were combusted at 460°C for 6 hours. The PTFE centrifuge tubes and
484 their caps were soaked in 1M HCl followed by a 1M NaOH bath, rinsed with distilled (DI water), and then
485 18 MΩ·cm Milli-Q (MQ) water. Each precipitation was carried out in a glove-box (818-GB, Plas-Labs Inc.)
486 under an N₂-atmosphere. An O₂-detector (Model 201 Portable Oxygen Analyzer, Quantek Instruments
487 Inc.) was employed to ensure an O₂-free environment was maintained (detection limit = 0.1% O₂). All pH
488 measurements were made using a Fisherbrand Accumet AB15 Basic pH Meter, calibrated using pH 4.00,
489 7.00, and 10.00 buffers.

490 **2.1 Sediment Sampling and Analysis**

491 **2.1.1 Study Area**



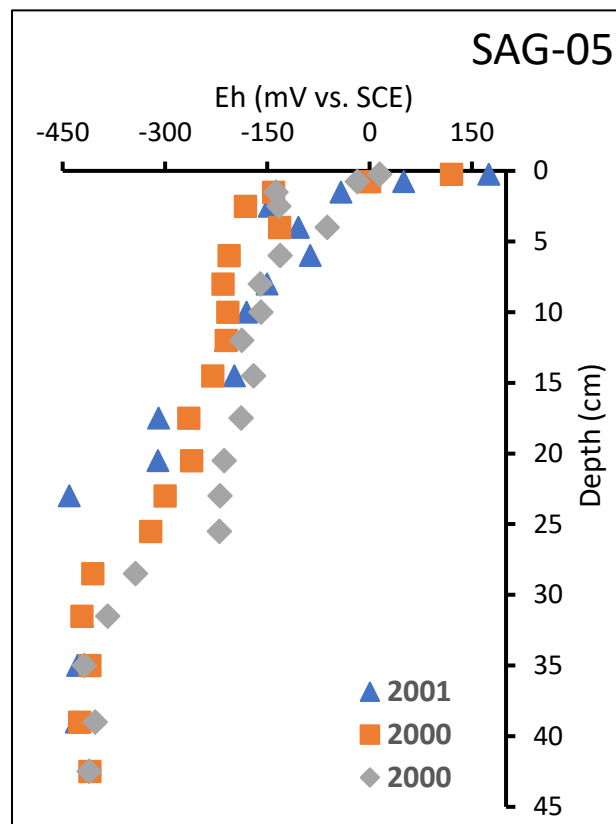
495 **Figure 2.1 (previous page):** A map showing the geographical location of the St. Lawrence River and
496 Saguenay Fjord. The difference in environment for stations SAG-05 and STN-23 are apparent; OM at
497 SAG-05 is more of a terrestrial origin, compared to the more marine origin at STN-23.

498

499 The St. Lawrence Estuary (SLE) is located in eastern Canada and is one of the most productive and
500 largest estuaries in the world. It connects the St. Lawrence River and the Saguenay Fjord with the Gulf of
501 St. Lawrence and ultimately flows into the Atlantic Ocean (Figure 2.1). As the meeting place between the
502 freshwater coming from inland and the salty marine water coming from the ocean, it represents a
503 unique environment for a variety of biological and chemical species. There is a particularly strong
504 thermocline in the SLE due to the mixing of the water bodies, which influences the temperature of the
505 bottom water and in turn biological productivity. The surface water of the SLE is generally well
506 oxygenated, but deeper into the water column oxygen becomes more sparse; recently in the Lower-SLE
507 (around Rimouski), bottom water oxygen levels have been found to be as low as 20% of saturation
508 (110). The decrease of O₂ in the SLE has been attributed to an increase in primary production driven by
509 nutrient inputs from land-runoff as well as an increase in water temperature from climate change, both
510 increasing biological demand for O₂ (bacteria-mediated reduction of chemical species such as sulfate,
511 nitrate, manganese, and iron occur readily).

512 Coastal areas, especially those that support a large
513 population such as the SLE, are known to have
514 relatively high inputs of OM into the water. OM
515 inputs in the SLE can be of two general sources;
516 terrestrial from the St. Lawrence River and the
517 Saguenay Fjord such as detritus from plants or
518 land-runoff, or from a marine source, such as
519 plankton.

520
521 **Figure 2.2:** The profile for reduction potential from
522 the sediment at station SAG-05 collected during
523 past sampling missions in 2000 and 2001.



524 Samples were collected from various sites but only the samples from two sites, shown in Fig. 2.1, will are
525 discussed in this study. The Saguenay Fjord sampling station SAG-05 ($48^{\circ}24'45.0''N$ $70^{\circ}49'15.6''W$), near
526 the Saguenay River outlet and about 90-m deep, is a unique station for a few reasons (111) that are
527 mainly a consequence of the relatively high sedimentation rate (up to 7 cm/yr) and the high terrestrial
528 OM inputs; the sediment pore water at this particular station is high in dissolved sulfide and OC
529 concentration. The high OM inputs from land result in high microbial activity, which increases the
530 demand for oxygen (through the oxidation of OM; respiration), decreasing the reduction potential even
531 at shallow depths in the sediment (< 1cm; Figure 2.2). This was visually obvious during the sampling
532 mission from the colour change from brown at the surface to black at depth (Figure 2.3), and olfactorily
533 evident from the strong sulfidic smell detected immediately after extraction (suggesting sulfate
534 reduction). The sampling station STN-23 ($48^{\circ}40'08''N$ $68^{\circ}44'02''W$) was also chosen for this study, as
535 another station showing significant (non-zero) amounts of sulfide in pore water, as reported by
536 Edenborn and colleagues (112). The geographical location of STN-23 being in the St. Lawrence Estuary
537 means that the proportion of marine-derived OM at this location is much higher than at station SAG-05.
538 Sulfate reduction has also been shown through past research to be active at this site (112).

539 **2.1.2 Removal of Sediment from the St. Lawrence River and Saguenay Fjord**

540 Sediment and water samples were obtained during June of 2017 on the *R/V Coriolis II*, a research vessel
541 operated by Reformar Inc. Sediment was removed from the sampling site using a box-coring apparatus.
542 This device can extract a rectangular cube of sediment from a
543 location with minimal disturbance. Once the box of sediment
544 was removed, it was placed in an on-board glove box (113)
545 which was then flushed with N_2 gas. The concentration of O_2
546 in the glove box on the Coriolis II was monitored and the
547 sediment was manipulated only after $[O_2] < 0.5\%$. The front
548 cover of the sediment box was lowered at specific intervals to

Figure 2.3: The box-core of sediment removed at station SAG-05 shows the obvious transition from oxic sediment (top) to anoxic (sulfidic) sediment at the bottom.



549 control the depth of the slice. The sediment core was sliced at a resolution of 0.5 to 5 cm, with the
550 higher resolution at the sediment-water interface and the lower resolution deeper in the core. Sediment
551 was collected from the surface to a depth of 42 cm into the sediment, and the sediment from the
552 precise depth range was placed into a 50-mL polypropylene centrifuge tube. The capped tube of
553 sediment was removed from the glove box, centrifuged at a speed of approximately 3000 g for 10
554 minutes, and then returned to the box and kept under N₂ atmosphere. The aqueous phase was removed
555 with a syringe and subsequently filtered through a 0.7 µm polyvinylidene difluoride (PVDF) membrane
556 filter for further analysis. The solid phase was immediately frozen at -20°C and remained frozen until
557 analysis upon return to the laboratory.

558 **2.1.3 Chemical Analysis of Pore Water**

559 The filtered pore water was analysed spectroscopically in the laboratory on-board the Coriolis II for
560 chemical species that are redox active (i.e. sensitive to O₂). Calibration curves were performed each day
561 of analysis. Chemical analysis for sulfide was performed according to the Cline method (114); briefly,
562 1000 µL of the filtered pore water was mixed with 1000 µL of diamine reagent, which was a mixture of
563 N,N-dimethyl-p-phenylenediamine sulfate and FeCl₃ in 50% (v/v) HCl. This solution was mixed and after
564 20 minutes the absorbance was measured in a spectrometer at 670 nm. The Cline method is typically
565 reported as applicable between the range of 0.03-32 mg/L and has a precision of + 2% at 95%
566 confidence level (114). Dissolved sulfate was measured using the turbidimetric method (115); 1500 µL of
567 filtered pore water was mixed with 300 µL sodium acetate buffer (containing MgCl₂ and KNO₃), which
568 was poured into a 2-mL microtube containing 0.2 g BaCl₂. When sulfate reacts with barium chloride,
569 barium sulfate is precipitated, which increases the turbidity of the sample to an extent that correlates to
570 the concentration of sulfate in the sample. This combination is shaken for 60 seconds and then the
571 absorbance is measured at 420 nm.

572 Dissolved ferrous iron was measured using the 1,10-phenanthroline method (116); 1000 µL of the
573 filtered pore water was mixed with 20 µL HCl, 600 µL of the phenanthroline solution, and 400 µL of an
574 ammonium acetate buffer. This solution was mixed and measured spectrophotometrically after 5
575 minutes at 510 nm. After the pH of the remaining filtered pore water from each depth was measured,
576 the solution was acidified to pH <2 with trace-metal grade HCl and refrigerated until analysis in the lab
577 for total Fe and Mn by inductively coupled plasma mass spectrometry (ICP-MS).

578 **2.1.4 Chemical Analysis of Solid-Phase**

579 Analysis of the frozen solid-phase was done after thawing the samples in the anoxic chamber. A 0.5 g
580 portion of the wet sediment was analysed for sulfur speciation as per a procedure developed by Couture
581 et al. (92). Briefly, three sequential extraction steps were carried out involving N₂ flowing through a
582 reaction vessel and trapping the evolved H₂S_(g) in two NaOH traps set up in series. The first extraction
583 targeted acid-volatile sulfides (AVS) which consists predominantly of FeS, and Fe₃S₄ (117–120). Under
584 constant stirring and a stream of N₂, gaseous hydrogen sulfide was produced after the addition of 6N
585 HCl and ascorbic acid (to prevent re-oxidation). The next extraction was aimed at the chromium-
586 reducible sulfur (CRS) fraction (pyrite, FeS₂); a Cr(II) solution was added to the sediment slurry,
587 reductively dissolving the pyrite, and the corresponding moles of H₂S_(g) bubbled through into the NaOH
588 traps. The third and final extraction targeted elemental sulfur (ES, S⁰), through the reaction between the
589 sediment and dimethylformamide (DMF). The two NaOH traps for each extraction were measured
590 spectrophotometrically using the Cline method (as described above in section 2.1.3)

591 **2.2 Isotherms**

592 **2.2.1 Sources and Treatment of Organic Matter**

593 Each type of natural organic matter (NOM) was extracted from its source using distilled water by shaking
594 and sonication. The solutions of NOM were filtered through a pre-combusted 0.7 µm GF/F filter. The
595 solution of planktonic OM was produced from phytoplankton (*Nannochloropsis*) purchased from Reed
596 Mariculture, which was repeatedly frozen under N₂ and thawed, then centrifuged, and the resulting
597 supernatant was filtered and used. The soil OM was leached in DI water from the soil of a compost bin.
598 The corn OM was a product of blended corn leaves with DI water. The concentrations of the NOM
599 solutions were measured using a Shimadzu Total Organic Carbon analyzer, which has an error of ±5%.

600 **2.2.2 Precipitation and Analysis of FeS**

601 Sodium sulfide nonahydrate (SIGMA #208043) and iron (II) chloride tetrahydrate (SIGMA #44939) were
602 both acquired from Sigma Aldrich. Solutions of 0.57 µM of each were prepared in MQ water
603 immediately before each precipitation experiment. For the isotherm modeling adsorption, FeS was
604 precipitated in MQ water before the NOM was added to the solution. The concentration of Fe²⁺ and S²⁻
605 in solution was chosen to remain within a reasonable concentration with respect to natural sediment,
606 and to precipitate roughly 0.05 g FeS.

607 In the case of the co-precipitation isotherms, 1 mL of the sulfide solution was added to the NOM
608 solution (final $[\Sigma H_2S] = 0.00228 \text{ M}$) and mixed before 1 mL of the ferrous iron solution was added (final
609 $[Fe^{2+}] = 0.00228 \text{ M}$). The pH of all samples was adjusted to ~ 7.5 if needed with NaOH. The NOM was
610 added for the final concentrations ranging from 0 to 0.023 M OC, corresponding to an OC:Fe ratio in
611 solution of 0 to 10. The identity of FeS precipitated without NOM was confirmed by XANES (see in
612 results section 3.5). Once the FeS was precipitated in solution, it was mixed by vortex and then let to
613 rest for 24 hours under N_2 atmosphere. The settled FeS precipitate was removed after rinsing and
614 centrifugation (3 times), freeze-dried and prepared for analysis of its OC content using an Elemental
615 Analyzer (EuroVector model EA3024) coupled to an Isotope Ratio Mass Spectrometer (IsoPrime,
616 Manchester, UK). This setup is known as an EA-IRMS. The FeS precipitates were weighed on a
617 microbalance (Mettler-Toledo) into a tin weighing boat, and the boat was closed for analysis.

618 **2.2.3 Calculation of Binding Coefficients from Isotherms**

619 Basic isotherm theory for adsorption adheres to the principle that there is a reversible equilibrium
620 between the free adsorbate (what is adsorbed), the free adsorbent, and the adsorbate-adsorbent
621 complex. In this experiment, DOM and FeS are considered the adsorbate and adsorbent, respectively. A
622 mass action law can be written for this relationship:

$$623 K_{ads} = \frac{[FeS \cdot DOM]}{[FeS][DOM]} \quad (1)$$

624 The total concentration of binding sites can be considered as the sum of the unbound sites on the
625 adsorbent and the sites that are occupied by the adsorbate:

$$626 [FeS_T] = [FeS] + [FeS \cdot DOM] \quad (2)$$

627 In addition, the mass of adsorbate sorbed per gram of adsorbent and the maximum monolayer coverage
628 of the adsorbent can be calculated and are represented as q_e and Q_o , respectively:

$$629 q_e = \frac{[FeS \cdot DOM]}{g FeS} \quad Q_o = \frac{[FeS_T]}{g FeS} \quad (3,4)$$

630 Experimental isotherms are obtained by plotting C_e , the equilibrium concentration of adsorbate in
631 solution (mg/L), against q_e (mg/g), the amount of adsorbate sorbed per gram adsorbent. Model
632 isotherms can be computed using linear regression (in the case of a two-parameter model) to find the
633 equation constants, and then by using the experimental C_e (the concentration of adsorbate at
634 equilibrium) to find the model q_e . Another strategy is to use Microsoft Excel's Solver module to find the
635 model parameters which minimize the difference between the model q_e and the experimental q_e . Each

636 model operates on several assumptions that are a consequence of the model equation. In this study,
637 three isotherm models were applied to the system; the Langmuir isotherm, the Freundlich isotherm,
638 and the Redlich-Peterson isotherm.

639 The Langmuir isotherm (121) has been widely re-appropriated from its original propose of modelling gas
640 to solid-phase sorption, and is currently used in areas extending past chemistry to model an equilibrium
641 between a liquid adsorbate and solid adsorbent. This model assumes monolayer coverage (a layer of
642 one molecule thickness of adsorbate on adsorbent), no inter-adsorbate interactions, and that each
643 binding surface on the adsorbent surface has equal affinity for the adsorbate (122). The Langmuir
644 equation is as follows:

$$645 \quad q_e = Q_o \frac{K_L C_e}{1 + K_L C_e} \quad (5)$$

646 For the purpose of this experiment, q_e describes the amount of DOM sorbed onto FeS (mg DOM/g FeS),
647 Q_o is the maximum amount of surface sites for sorption per g FeS (mg DOM/g FeS), K_L represents the
648 Langmuir isotherm constant (dm^3/mg), and C_e is the concentration of DOC in solution at equilibrium
649 with FeS (mg/L). The Langmuir equation may not be valid for the sorption modelled in this experiment
650 because the naturally-derived adsorbate contains a complex mixture of carbon functionalities, with
651 unknown but certainly varying affinities for the FeS adsorbent. In addition, the sorption cannot be
652 assumed to be monolayer. If the experiment does not abide by the assumptions, we cannot say that K_{ads}
653 = K_L , but we can compare K_L across the types of DOM; a higher K_L denotes a higher affinity of FeS
654 towards the DOM.

655 The Freundlich model (123) was originally developed for sorption between charcoal and an adsorbate. It
656 describes sorption that is not limited to a monolayer (non-uniform), that is non-ideal and reversible
657 (124, 125). Theoretically from this model, the binding sites with the strongest affinity are occupied first,
658 resulting in a decreasing adsorption energy throughout the sorption process (126). The Freundlich
659 equation is expressed in equation 6:

$$660 \quad q_e = K_F C_e^{\frac{1}{n}} \quad (6)$$

661 Here q_e describes the amount of DOM sorbed onto FeS (mg DOM/g FeS), C_e is the concentration of DOC
662 in solution at equilibrium with FeS (mg/L), K_F represents the Freundlich isotherm constant (mg/g)
663 (dm^3/g)ⁿ, and n is the adsorption intensity which can also infer surface heterogeneity (closer to zero =
664 more heterogeneous).

665 The Redlich-Peterson isotherm (127) incorporates both the Langmuir and Freundlich models. It is a
 666 notably versatile model that tries to describe sorption over a large range of adsorbate concentration; at
 667 low concentration, it tends towards the Langmuir model and at high concentration it tends towards the
 668 Freundlich model. The Redlich-Peterson equation uses three parameters, as opposed to two, as can be
 669 seen in equation 7:

$$670 \quad q_e = Q_o \frac{K_R C_e}{1 + \alpha_R C_e} \quad (7)$$

671 In the Redlich-Peterson model the variables are as follows: Q_o is the maximum monolayer coverage
 672 (mg/g), K_R is the Redlich-Peterson isotherm constant (L/g), and α_R is the Redlich-Peterson isotherm
 673 constant (1/mg). For this isotherm model, a minimization procedure in Microsoft Excel using the Solver
 674 add-in must be employed to solve for the variables.

675 Error functions are used to evaluate the fit of each isotherm onto the experimental data. The functions
 676 used in this study are presented in Table 2.1.

Error Function	Equation	Limitations
Sum of standard deviations (SSD)	$\sum_{i=1}^n (q_{e,calc} - q_{e,meas})_i^2$	Bias towards higher concentration observations (128)
Nonlinear chi-square test (χ^2)	$\sum_{i=1}^n \frac{(q_{e,calc} - q_{e,meas})^2}{q_{e,meas}}$	χ^2 values may be subjected to significant uncertainty for non-linear models (129)
Sum of absolute error (EABS)	$\sum_{i=1}^n q_{e,meas} - q_{e,calc} $	Bias towards higher concentration observations (128)

677 **Table 2.1:** The equations for the error functions used to evaluate the three isotherm models used in the
 678 study.

679 **2.3 Scanning Electron Microscopy**

680 Samples were precipitated with and without soil OM. The effect of lyophilization was tested by imaging
 681 samples dried in a vacuum and dried by lyophilization. A FEI Quanta 450 Environmental Scanning
 682 Electron Microscope (FE-ESEM) was used for the imaging, with Pt coating prior to analysis. Samples were
 683 imaged from a magnification of 300x to 200,000x.

684 **2.4 Dithionite-Citrate Buffer Reduction (DCB) Method**

685 The effect of OM on the reactivity of FeS towards O₂ was evaluated by employing a method that
686 dissolves oxidation products of FeS: Fe oxides. The concentration of Fe oxides can be directly measured,
687 corresponding to the extent of oxidation.

688 FeS precipitates were prepared through co-precipitation with dissolved OM extracted from corn leaves
689 and OC:Fe ratios of 0 to 10. The precipitates left in solution, let to oxidize at standard temperature and
690 pressure (STP) for 48 hours, before being lyophilized. The samples were treated according to the
691 method described in Lalonde et al. (130). Briefly, a solution of 0.11 M sodium bicarbonate and 0.27 M
692 trisodium citrate (replaced by a 1.6 M sodium chloride solution for the control to adjust ionic strength)
693 was added to 0.15 g of sample in a Teflon tube. It was capped and heated to 80°C, at which point
694 sodium dithionite (sodium chloride for the control) was added, and then kept at 80°C for 15 minutes.
695 The tubes were centrifuged at 3000 G for 10 minutes, after which the solid fraction was rinsed with
696 distilled water three times. The supernatant and rinses were combined, acidified, and filtered on a pre-
697 combusted GF/F filter (0.7-μm nominal pore size).

698 The concentration of dissolved Fe in solution was measured by ICP-MS using external calibration
699 (Agilent), and the actual concentration of OC in the freeze-dried FeS precipitate was measured using EA-
700 IRMS. Each precipitation and oxidation was performed in duplicate.

701 **2.5 Synchrotron X-ray**

702 Synchrotron X-ray analysis of synthetic FeS precipitates (with and without OM) and of anoxic sediment
703 from the June 2017 sampling mission, was done by a collaborator, Dr. Aude Picard, at the Advanced
704 Light Source (ALS) at the Lawrence Berkeley National Laboratory in California (beamline 11.0.2) and at
705 the Canadian Light Source (CLS) in Saskatchewan (beamline 10 ID-1). The specific technique of scanning
706 transmission X-ray microscopy (STXM) is used to look at the atomic composition of individual particles
707 through the analysis of “pixels” of about 30 nm by 30 nm. X-ray absorption happens when the incident
708 photon energy is higher than the energy needed to ionize an electron from in inner-shell orbital. Near
709 edge X-ray fine structure (NEXAFS) absorption spectroscopy involves energy that is just below the
710 ionization energy, therefore the electron is promoted to unoccupied or partially occupied orbital. The
711 near-edge adsorption energies are used to infer the local chemical environment of the atom in question
712 (131). For example, electron withdrawing/donating groups substituted in or on aromatic rings
713 increases/decreases the absorption energy of the 1s electron on C (132). Pre-edge absorption features

714 are also affected by variations in valence state. This is due to the electrostatic effect resulting from the
715 increased binding energy as the valence increases (133, 134). The ligands attached to a metal ion also
716 influence the charge of the ion which influences the absorption energy (134). Each pixel of the sample is
717 analysed with STXM/NEXAFS, resulting in maps of the particles showing where the absorption is highest
718 and lowest for the incident photon energy. X-ray absorption near edge structure (XANES) spectroscopy
719 at the Fe and S L-edges was also carried out to confirm the identity of FeS. A background subtraction of
720 the pre-edge image was employed, producing maps for specific oxidation states and forms of elements.

721 STXM/NEXAFS can be considered a good technique for observing the correlation on a particle level
722 between a metal ion of specific valence, and the functional groups associated to it. The pairing of these
723 two techniques has been used countless times on samples of natural origin such as soil (26, 135–137),
724 marine particles (132), and iron oxides (138). Although organic material is hard to examine using
725 STXM/NEXAFS because of the microscale spatial heterogeneity (26, 131, 135, 137), it remains one of the
726 only techniques for observing co-localization and elucidating the structure of OM at the nanoscale. Here
727 we used STXM/NEXAFS to look for spatial association between the Fe atom of synthetically prepared
728 FeS, and C functionalities from OM originating from corn leaves. Certain C functionalities that we expect
729 to see are those of aromatic C (285 eV), amide C (288.2 eV), carboxylic C (288.6 eV), and carbonate C
730 (290.3 eV). We can also use NEXAFS to confirm that the FeS prepared has not been oxidized to a
731 significant extent during preparation, storage, and transport. Using STXM/NEXAFS on the anoxic
732 sediment samples, we can observe which C functionalities were co-localized with the particle, and
733 possibly identify the source of the OM.

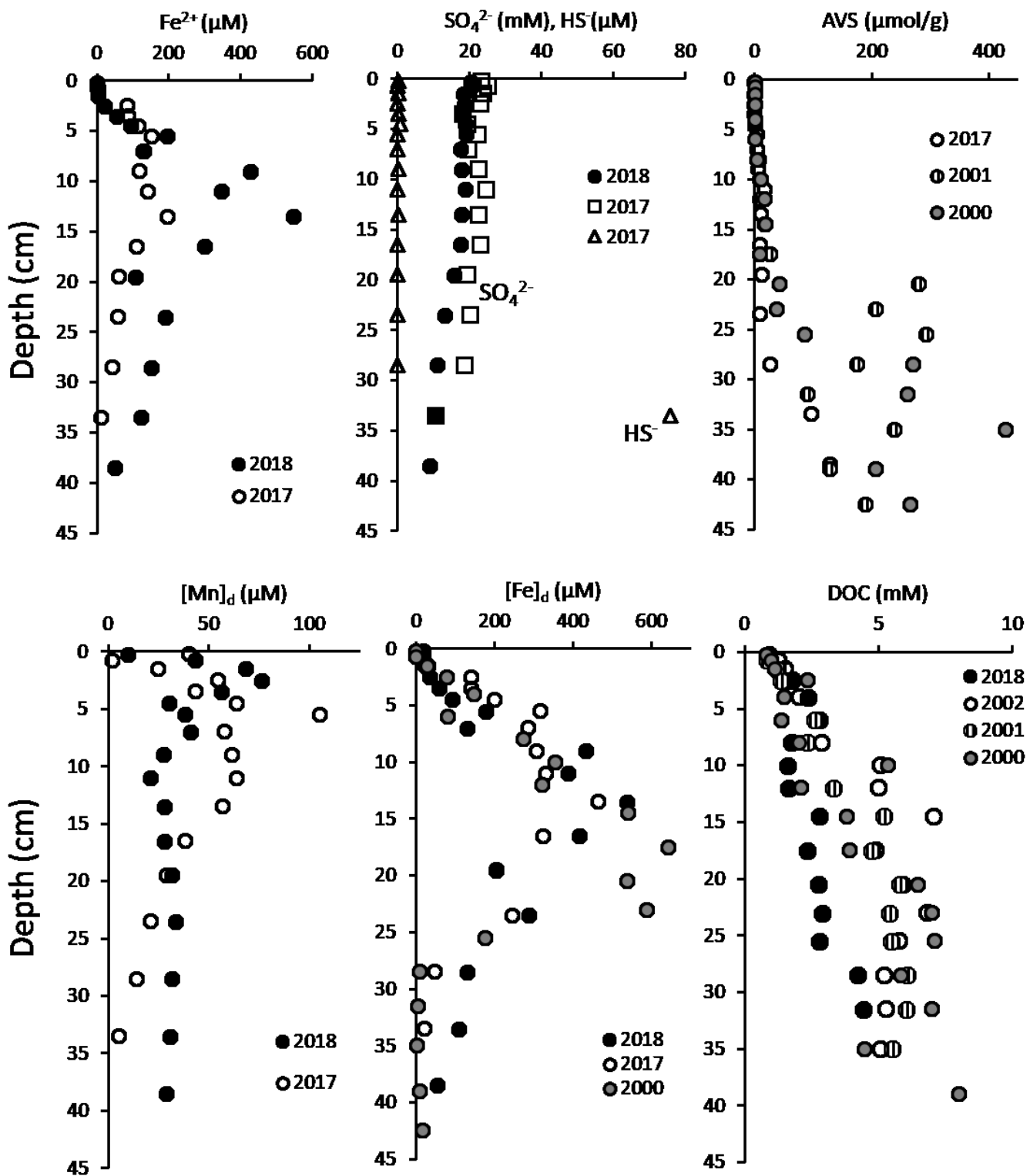
734

735 **3 Results**

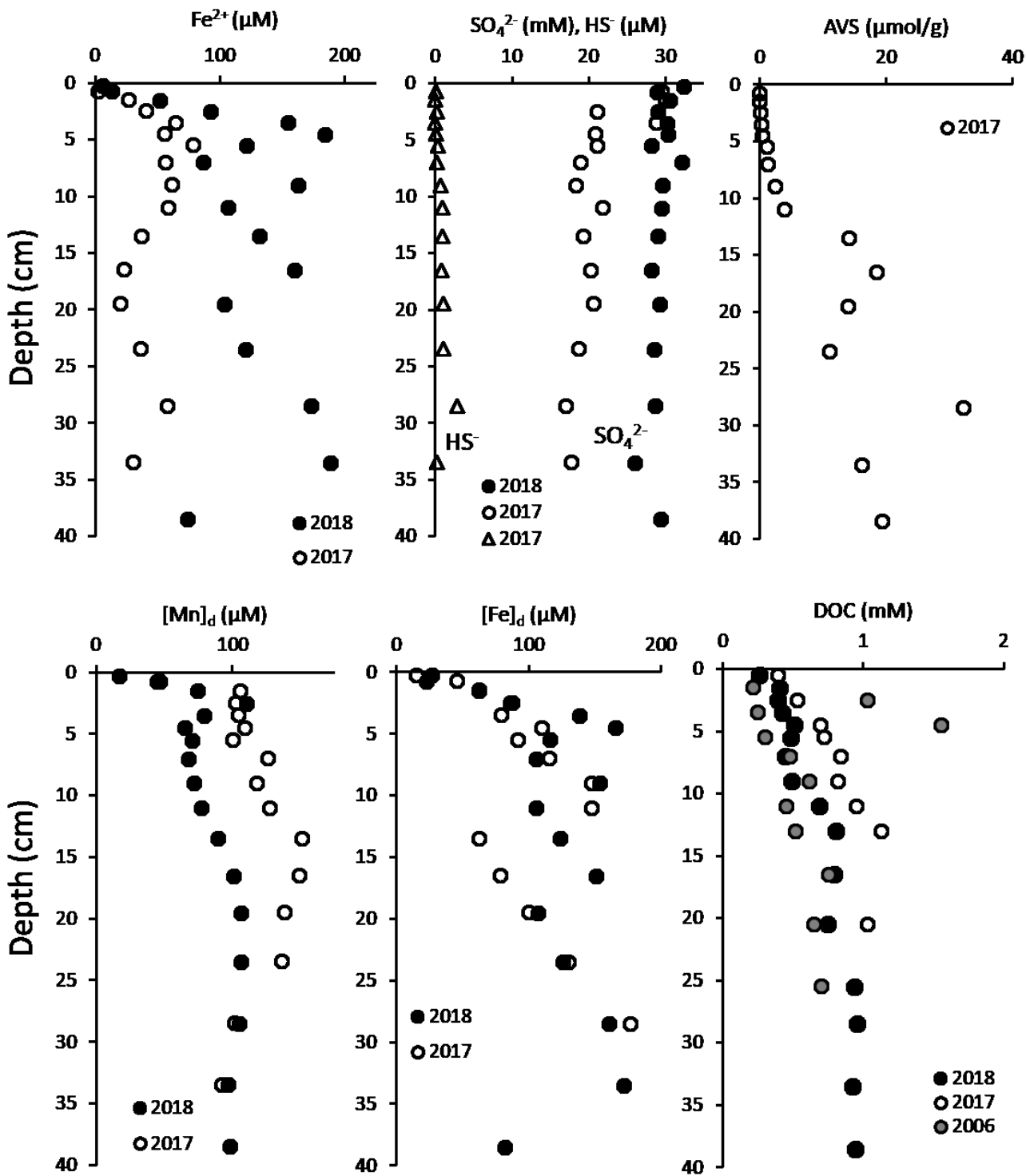
736 **3.1 Chemical Speciation Profiles for the Saguenay Fjord and St. Lawrence Estuary**

737 Sediment pore water and solid-phase chemical species profiles from the sampling missions of 2017 and
738 2018 for the two stations of interest, SAG-05 and STN-23, are shown in Figures 3.1 and 3.2, respectively.
739 Additional years for which concentrations are known from these stations are added to the results
740 obtained in this study. The results of chemical analysis on the pore water of station SAG-05 show a
741 similar profile for Fe(II) and total dissolved Fe. The ferrous iron pore water profiles show a bell-shaped
742 pattern; an increase in Fe^{2+} concentration from 0 cm to 8 cm, remaining stable until around 15 cm, and
743 then decreasing. The total dissolved iron profile shows a similar pattern, but with larger concentrations

744 **Figure 3.1:** Sediment profiles for station SAG-05. The data was acquired for this study during the
 745 summers of 2017 and 2018. Additional data was added to this figure from sampling missions in 2000,
 746 2001, and 2002. Note the labels for SO_4^{2-} and HS⁻. $[\text{Fe}]_d$ consists of dissolved Fe(II) and Fe(III).



747 **Figure 3.2:** Liquid and solid-phase profiles for STN-23 from sampling missions during the summers of
 748 2017 and 2018. Data from older years (past missions- data obtained by past students) added. Note the
 749 labels for SO_4^{2-} and HS⁻. $[\text{Fe}]_d$ consists of dissolved Fe(II) and Fe(III).



750 overall and with the concentration peak further downcore. It is expected to see an accumulation of pore
751 water Fe²⁺ below the zone of Fe oxidation (the mobilization of Fe is a result of the reductive dissolution
752 of Fe oxides, as discussed in Section 1.2), but this iron is removed from the pore water downcore
753 through the precipitation of FeS.

754 Sulfate profiles (the circles) for SAG-05 steadily declined downcore in 2018, while the year 2017 profiles
755 showed a strong decrease only deeper than 20 cm. From the sediment-water interface to a depth of 35
756 cm, dissolved sulfate in the pore water decreased by only 50%, from about 25 mM to 12 mM. This
757 decrease in sulfate was expected for a sediment with obvious sulfate-reducing bacteria activity, but
758 compared to a study done in 1995 at the same sampling station by Gagnon *et al.* (111), our sulfate
759 concentration at depth showed a higher concentration by about one order of magnitude, although we
760 used the same method (BaSO₄ precipitation). At the same depth where we see the lowest concentration
761 of sulfate at SAG-05, we also see an accumulation of dissolved sulfide (the triangles in Figures 3.1 and
762 3.2) in the pore water, to about 70 µM. Looking at the solid-phase results for SAG-05 in Figure 3.1, the
763 region of increased acid-volatile sulfide (AVS) and other sulfur species corresponds to the removal of
764 pore water iron, which begins at around 20 cm. The formation of AVS in the sediment is probably
765 responsible for the removal of dissolved Fe from solution, by the mechanisms of Fe(II) precipitating with
766 sulfide as iron-sulfide species such as FeS or Fe₃S₄. The precipitation of AVS also corresponds to the
767 stabilization of pore water DOC concentrations that is seen at approximately 20 cm.

768 At station SAG-05 the pore water profiles for 2017 and 2018 show that the region with the highest
769 manganese concentrations is the closest to the sediment-water interface. This is consistent with what
770 was seen in 1995 at SAG-05 by Gagnon *et al.* (111). An initial accumulation of liquid-phase Mn followed
771 by a concentration decrease further down into the core can be indicative of oxygen-poor conditions,
772 which keep Mn reduced and dissolved in the aqueous-phase, allowing for the diffusion upwards of
773 dissolved Mn(II), where it is typically re-oxidized into a manganese oxide (139) or precipitated as
774 manganese carbonate (140). The dissolved Mn profile for STN-23 (Figure 3.2) shows a slightly different
775 trend; an accumulation in the top 2 cm of the sediment, followed by a slow concentration increase until
776 15 cm, before stabilizing downcore (2018) or decreasing from 25 cm downcore (2017). Comparing the
777 Mn profiles of the two stations, we see that overall there is the similar trend of a peak about 2 cm into
778 the core, in 2017 both stations show a decrease at depth, but the concentrations at STN-23 are about
779 double that at SAG-05. Measurements of dissolved manganese in pore water may be an indicator of
780 microbial activity; as Mn (IV)/(III) is used as an electron acceptor, releasing Mn(II) to the pore water

781 through reductive dissolution. From this perspective, the Mn profiles suggest that the sediment solid-
782 phase at STN-23 is enriched in reducible Mn minerals compared to SAG-05, as reported previously (141).

783 Unlike the SAG-05 profile, removal of Fe from the liquid phase is not seen at STN-23, at a depth that
784 corresponds to the increase of AVS in the solid phase, which starts at about 12 cm. The iron profiles at
785 STN-23 show an accumulation in the first 5 cm from the sediment-water interface, but further downcore
786 it is difficult to conclude on one pattern due to the differences between sampling years. The sulfate
787 profiles at STN-23 are generally stable downcore, and the same is seen for the sulfide profile; the
788 concentration is low, only showing a detectable concentration at around 30 cm. At this depth we see a
789 slight increase in dissolved sulfide, with a slight decrease of sulfate, likely corresponding to the sulfate
790 reduction zone. The five-fold difference in DOC concentrations between the two stations results in a
791 higher rate of microbially-mediated sulfate reduction, which promotes precipitation of AVS (142, 143),
792 which is about 10-times more concentrated at station SAG-05.

793 **3.2 Sorption and Co-precipitation of NOM on Synthetic FeS**

794 **3.2.1 Sorption Isotherms and Constants**

795 Under O₂-free conditions, FeS was precipitated before introduction to OM (adsorption) and while in the
796 presence of OM (co-precipitation), and the resulting isotherms are shown in Figure 3.3. The slope of the
797 initial isotherm curve at low concentrations of [DOC] (low C_e) demonstrates the initial affinity of FeS
798 towards the specific type of OM, and the plateau at higher concentrations of OM (high C_e) represents
799 the maximum sorption capacity of the solid. Adsorption curves are a similar shape for all three types of
800 OM, while the co-precipitation isotherms show a similar shape for plankton and soil, but the corn OM
801 curve appears to have yet to reach maximum sorption capacity. Overall the experimental data shows
802 that co-precipitation results in a larger sorption capacity than adsorption, and that FeS can sorb
803 plankton OM with the highest affinity and capacity compared to soil and corn OM. Soil OM consistently
804 has the lowest sorption capacity between the types of OM, and this can be attributed to the
805 composition of this OM; it has been exposed to atmospheric oxygen and bacteria for a significantly
806 longer time than plankton and corn OM, and therefore may be less reactive. Error bars representing the
807 standard deviation for the three replicate precipitations are largest for corn and plankton over the two
808 types of sorption. A reason for the large error bars for these OM types specifically may be variability
809 within the OM source over the time period of the experiment; corn and plankton OM contain molecules
810 that have yet to be exposed to bacteria (unlike soil OM), and therefore are more susceptible to
811 degradation over time (despite being stored at 2°C in a closed container).

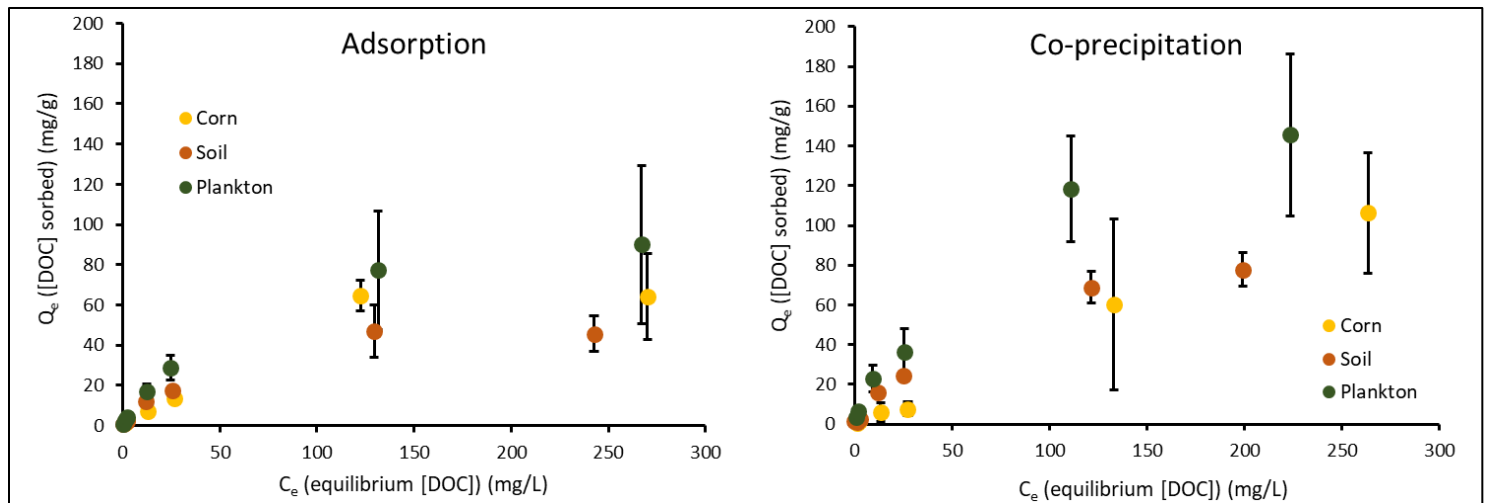


Figure 3.3: Adsorption and co-precipitation isotherms from the experimental data showing the amount of DOC sorbed by FeS for corn, soil and plankton OM.

812

813

	OM type	Langmuir			Freundlich		
		Q_o	K_L	R^2	n_F	K_F	R^2
Adsorption	Corn	70.522	0.021	0.439	1.138	0.687	0.983
	Soil	49.875	0.038	0.980	1.622	2.011	0.985
	Plankton	95.877	0.018	0.995	1.375	2.104	0.980
Co-precipitation	Corn	204.499	0.004	0.259	1.393	0.991	0.801
	Soil	99.206	0.018	0.832	1.545	2.414	0.804
	Plankton	159.236	0.020	0.875	1.297	2.957	0.985

814

Table 3.1: Isotherm parameters and values of the coefficient of determination (R^2) obtained through linear regression of the Langmuir and Freundlich models. Q_o : max. monolayer coverage (mg/g), n_F : adsorption intensity, K_L : Langmuir isotherm constant (dm³/mg), K_F : Freundlich isotherm constant (mg/g)

817

818

819

820

821 Isotherm models are useful for examining solid-solute interactions and have applications extending past
822 geochemistry into biochemistry and chemical engineering. Models with the closest fit to the
823 experimental data can divulge information about the adsorbent's affinity towards the adsorbate, the
824 sorption mechanism, and the adsorbent's surface binding characteristics. Linear regression can be used
825 to determine the variables in two-parameter models (Langmuir and Freundlich) but cannot be used for
826 evaluating models with more than two parameters (Redlich-Peterson), thus computation in Excel
827 through error minimization is required. Several isotherm models were tested against the experimental
828 data, and the Langmuir, Freundlich, and Redlich-Peterson models were the ones with the closest
829 predicted values and underlying theoretical background matching that of our experiment. Models such
830 as the Dubinin-Radushkevich, Tempkin, and Flory-Huggins, which have been used in a solid-solute
831 context (128, 144), were rejected due to large variability between the predicted and experimental
832 results.

833 The constants found from the isotherms obtained from linear regression are shown in Table 3.1, models
834 fitted using linear regression show various degrees of agreement between the model and experimental
835 values. Overall, the results of linear regression suggest, using the coefficient of determination as the
836 measure, that the Freundlich model is a better fit to the experimental data. Consistently over the three
837 types of OM, the Langmuir model shows that co-precipitation results in more OC incorporated into the
838 aggregate for each respective OM source (seen from the Q_0 parameter), which is consistent with the
839 theory of this type of sorption (discussed in section 2.2.3). The Langmuir model also shows which types
840 of OM result in the lowest Q_0 (the maximum monolayer coverage of the adsorbent), and soil OM has the
841 lowest value for monolayer coverage over both types of sorption. Soil OM is the most decomposed out
842 of these three OM types, and that may result in smaller molecules with a more refractory (less reactive)
843 nature. The isotherm constants (K_L and K_R) can be used within each model as a measure of the affinity of
844 FeS for each OM source. Results from the linear regression of the Freundlich model suggest that FeS has
845 and almost equal affinity for soil and plankton OM by adsorption, and the highest affinity for plankton
846 OM by co-precipitation. Corn OM perhaps consists of the largest molecules out of the three types of OM
847 used in this study, thus despite FeS having a larger binding capacity for corn than soil OM, the sorption
848 affinity is lowest for corn perhaps because of the binding of these large macromolecules such as
849 cellulose.

850 Resulting graphs for the nonlinear analysis of the three isotherm models are shown in Figure 3.4, in
851 which the solid lines are of the experimental data and the dotted lines represent the models. From a

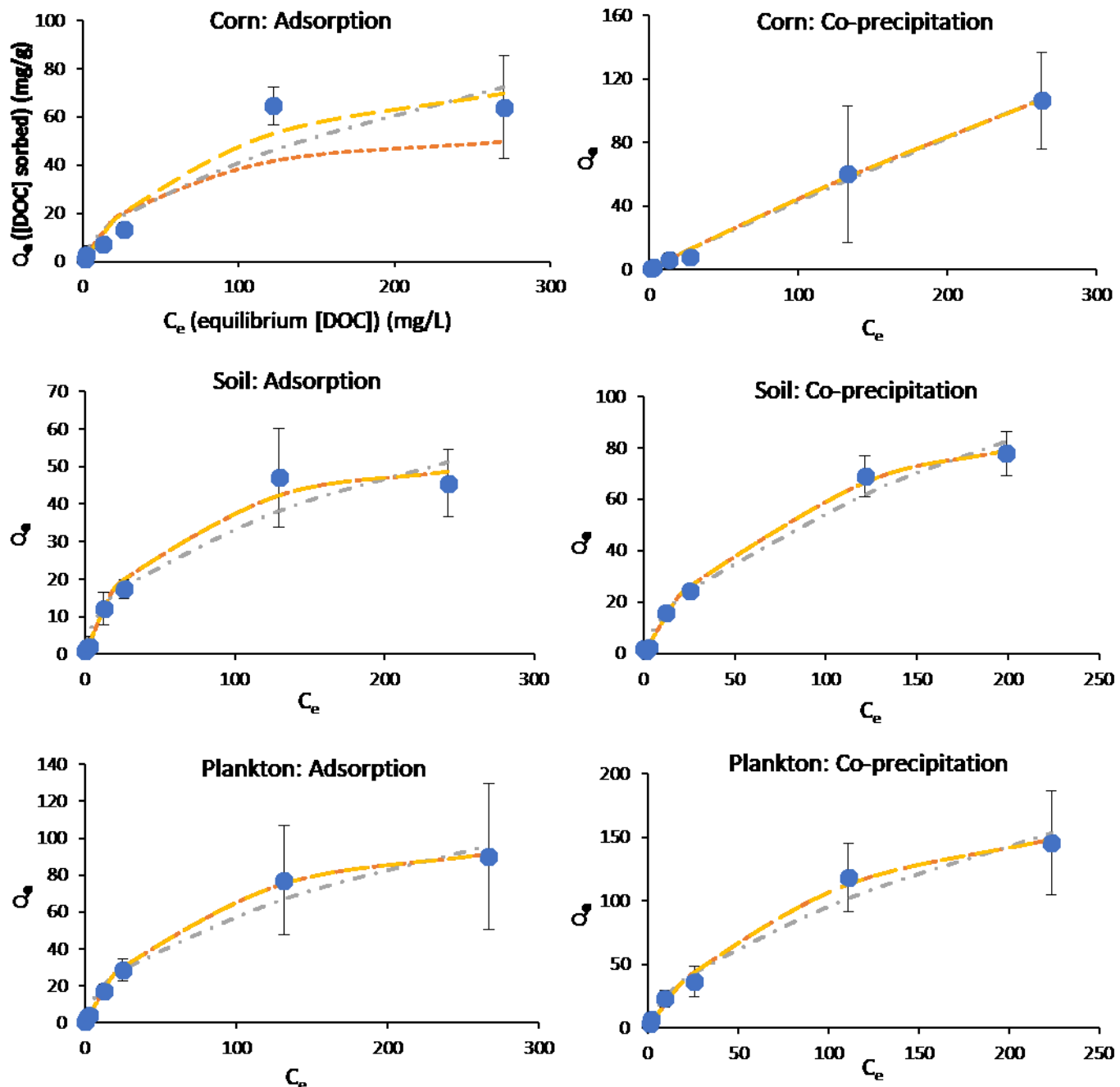


Figure 3.4: The experimental sorption isotherms compared to the Langmuir, Freundlich, and Redlich-Peterson model isotherms (see legend at right). The x-axis in the above graphs shows C_e (mg/L), the concentration of DOC in solution at equilibrium with FeS, and the y-axis shows Q_e (mg/g), the mass of DOC associated to the FeS precipitate.

- Experimental
- - - Langmuir
- - - - - Freundlich
- — — Redlich-Peterson

	Langmuir					Freundlich					
	Parameters		Error Functions			Parameters		Error Functions			
	OM type	Q _o	K _L	SSD	χ ²	EABS	n _F	K _F	SSD	χ ²	EABS
Adsorption	Corn	85.99	0.0154	807.17	17.927	50.804	1.78	3.10	495.21	20.061	46.518
	Soil	58.84	0.0199	39.51	2.040	12.907	2.15	3.98	130.93	12.734	22.736
	Plankton	115.14	0.0143	8.89	0.643	6.596	1.97	5.64	181.74	17.569	29.219
Co-precipitation	Corn	768.52	0.0006	37.88	3.425	11.443	1.05	0.54	48.37	3.374	13.746
	Soil	111.36	0.0123	16.17	2.779	10.235	1.71	3.74	103.18	19.126	20.320
	Plankton	214.16	0.0100	118.75	3.720	24.175	1.72	6.58	417.14	10.352	43.527

853	854	855	856	857	858	859	860	861	Redlich-Peterson									
									Parameters									
									OM type	Q _o	K _R	α _R	SSD	χ ²	EABS			
Adsorption	Co-precipitation	Corn	Soil	Plankton	Corn	Soil	Plankton	Corn	Corn	1.734	0.578	0.0106	233.18	8.737	30.299			
									Soil	0.782	1.495	0.0199	40.13	2.041	12.905			
									Plankton	1.459	1.128	0.0143	8.89	0.642	6.596			
862	863	864	865	866	867	868			Co-precipitation			Corn	0.349	1.350	0.0006	37.88	3.417	11.453
									Soil	1.151	1.192	0.0123	16.17	2.779	10.235			
									Plankton	1.630	1.319	0.0100	118.75	3.720	24.176			

Tables 3.2 and 3.3: Isotherm parameters and error functions values obtained for the Langmuir, Freundlich, and Redlich-Peterson (RP) models, computed using Microsoft Excel. The error functions are used to assess the compatibility of the fit of the model onto the experimental data. Q_o: max. monolayer coverage (mg/g), K_L: Langmuir isotherm constant (dm³/mg), n_F: adsorption intensity, K_F: Freundlich isotherm constant (mg/g), K_R: RP isotherm constant (L/g), α_R: RP isotherm constant (1/mg). The error functions are sum of squared deviation (SSD), chi-squared (χ²), and the sum of absolute error (EABS).

869 general visual inspection of the models, it is apparent that the Redlich-Peterson model, which employs a
870 Langmuir-type approach at low adsorbate concentrations and a Freundlich-type approach at high
871 adsorbate concentrations, is the most suited to adapt to the experimentally obtained data. The results
872 of the three error functions computed (Tables 3.2 and 3.3) agree with this visual observation. The “Q_o”
873 parameter attained from the Redlich-Peterson model describes the maximum monolayer capacity,
874 similar to the parameter of the Langmuir model. The values of Q_o obtained by the Redlich-Peterson
875 model are lower than those obtained by the Langmuir model.

876 **3.2.2 Comparison of Error Function Values**

877 The constants and error function values obtained from the isotherms from both linear regression and
878 computational error minimization are shown in Tables 3.1, 3.2, and 3.3. There is considerable difference
879 in the parameters of each model attained by the two methods, attributed to the treatment and
880 manipulation of the data. The error functions give numerical representation to how well the model fits
881 the data. The error functions have limitations; notably the bias towards data points corresponding to
882 higher concentrations. In the case of these isotherms this bias may not be perilous because of the small
883 number of data points at the highest concentration.

884 **3.3 Characterization of FeS Precipitates by Scanning Electron Microscopy (SEM)**

885 The use of SEM provides a close look at the surface texture and structural morphology of the FeS
886 particles, allowing qualitative conclusions to be drawn on the effect of NOM on FeS precipitation. The
887 resulting SEM images reflect on NOM's influence on the size and surface texture of amorphous FeS. It
888 was visually apparent during the precipitations that the solutions with a higher concentration of OM
889 from a soil leachate flocculated into larger aggregates, and SEM was used to confirm this observation.
890 The effect of lyophilization on the aggregation of FeS was explored through imaging the particles at the
891 same OC:Fe ratio dried by lyophilization and dried in a vacuum. There was no significant difference
892 observed.

893 The images from SEM are shown in Figure 3.5, the left column images are of FeS precipitated without
894 OM, and the right column is of FeS precipitated in the presence of 40 µM soil OM (an OC:Fe ratio of
895 about 10). The images with the lowest magnification (A and D) clearly demonstrate that FeS precipitated
896 with NOM forms larger amorphous aggregates, approximately 5x larger. Besides encouraging larger
897 aggregates, the NOM influences the surface texture of the particles; FeS precipitated without NOM
898 formed particles with a relatively smooth surface while FeS precipitated with NOM resulted in particles
899 with a textured surface. The texture of the OM-influenced particles has a “flaky” quality that is

900 completely absent in the precipitates without OM. A study by Picard *et al.* looked at the influence of
901 sulfate-reducing bacteria on the formation of iron-sulfides and found a similar result (107); FeS and Fe_3S_4
902 had a different surface texture and formed larger aggregates when in the presence of the bacteria,
903 compared to an abiotic precipitation.

904

905

906

907

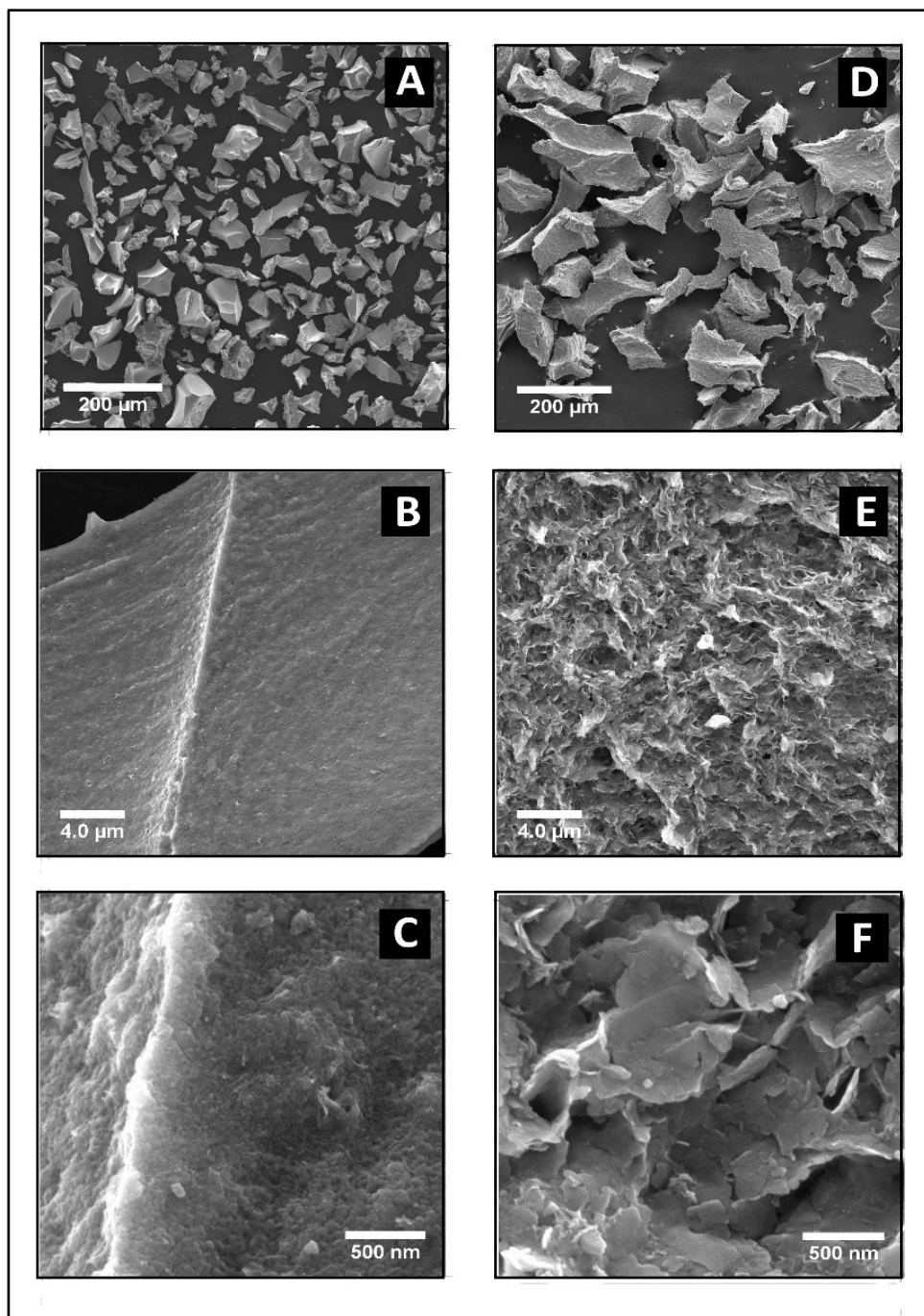
908

909

910

911 **Figure 3.5:** Scanning
912 electron microscopy
913 images of synthetic FeS.

914 Panels A to C are of FeS
915 precipitated in the
916 absence of OM, and
917 panels D to F are of FeS
918 precipitated in the
919 presence of a 40 μM soil
920 OM leachate.

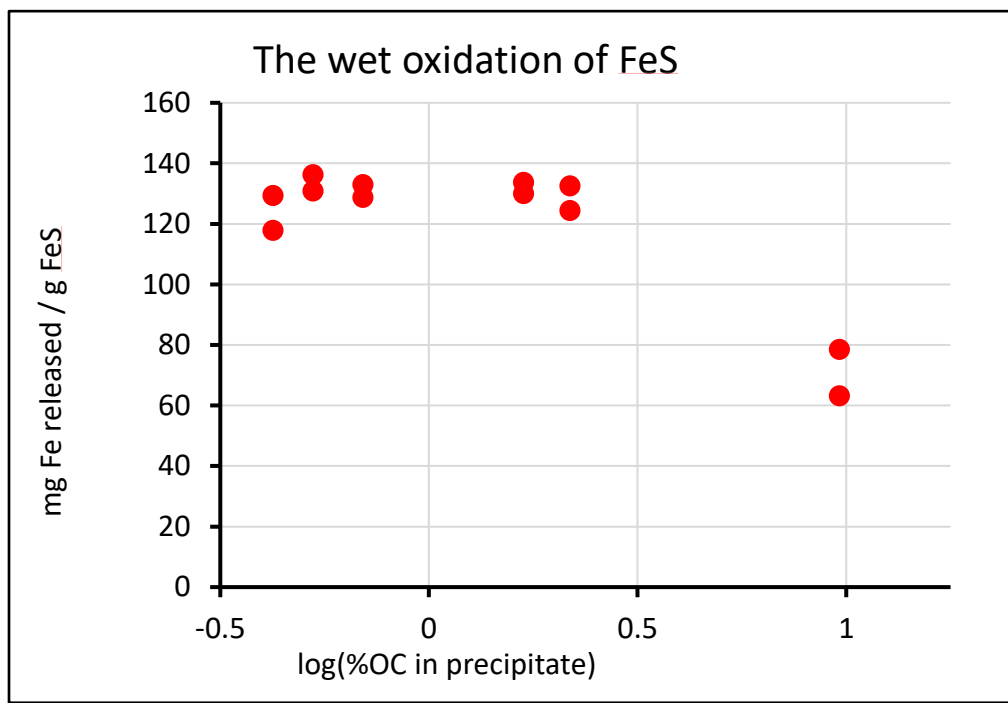


930 **3.4 Effect of Associated OM on FeS Oxidation**

931 The dithionite-citrate buffer reduction (DCB) method works by selectively dissolving reactive iron oxides.
932 This study employed a method that was slightly modified from the original, first introduced in 1960 (1).
933 Whether this method also targets AVS in the sample is unclear; several studies have claimed that AVS is
934 targeted along with amorphous and crystalline Fe(III) oxides (57, 145), however this may be a result of
935 lacking or insufficiently sustained O₂-free conditions, resulting in oxidation of Fe(II) species. To test
936 whether the DCB method targets FeS, the method was carried out on FeS precipitated without OM, kept
937 in O₂-free conditions before and after lyophilization. Iron in solution after reduction by the DCB method
938 was measured by ICP-MS, which quantifies the amount of Fe dissolved by the method. The results
939 demonstrate that in our conditions, the DCB method dissolved on average 4.98% ± 0.36% of our FeS,
940 possibly a consequence of O₂-exposure while moving the precipitate to and from the freeze-dryer.
941 Regardless, this result indicates that the DCB method can be used to quantify FeS oxidation.

942

943 **Figure 3.6:** The change in Fe(II) oxidized after exposure to atmospheric O₂, precipitated with varying
944 concentrations of OM. The x-axis is presented as a logarithmic scale of the amount of OC measured in
945 the precipitate and the y-axis shows the amount of Fe released per g of FeS.



957 By precipitating FeS with various NOM concentrations, exposing the precipitates in solution to
958 atmospheric O₂ for a determined period of time, and then using the DCB method with ICP-MS to
959 measure Fe(III) formed from FeS oxidation, the effect of NOM on the reactivity of FeS towards O₂ can be
960 evaluated. The data (Figure 3.6) exhibits a constant amount of FeS oxidation until a downward trend is
961 apparent at an OC:Fe ratio of 6.5, suggesting that NOM has a protecting effect on FeS oxidation in the
962 atmosphere only at high NOM concentrations. Although more data at high OC:Fe ratios is required to
963 confirm this result, it can be theoretically supported by a few mechanisms; NOM has a negative effect
964 on the surface area of FeS (a change in reaction-site density), NOM is occupying binding sites on FeS and
965 thus oxidized first, or NOM changes the degree of crystallinity.

966 **3.5 Characterization of Molecular Binding of OM on FeS**

967 **3.5.1 Synthetic FeS Precipitated with OM**

968 STXM/NEXAFS is one of the few techniques available for mapping the chemical heterogeneity of nano-
969 scale material. The STXM maps of synthetically prepared FeS exhibiting the elemental distributions of
970 Fe(II) and various C functionalities are shown in Fig. 3.7. On the left and right columns are the images of
971 the FeS that was co-precipitated and adsorbed, respectively, with planktonic OM. These images show
972 regions of high concentration (white areas) and of low concentration (black areas) of the chemical
973 species corresponding to the specific incident energy of each map. The top image of each column shows
974 the absorption for the particle area of Fe(II) at 708.7 eV, corresponding to the Fe L_{III}-edge (146, 147),
975 while the bottom images show the absorption of various C functionalities at the C 1s K-edge (135, 148).
976 Our method of FeS precipitation (as well as the O₂-free conditions) was confirmed to be adequate
977 through NEXAFS imaging of the Fe L_{III}-edge along with the comparison to spectra of reference material
978 (Figure 3.8). XANES was carried out at the S L-edge, but due to difficulties of the analysis, distinguishing
979 between FeS and pyrite (FeS₂) is not possible.

980 Organic matter is heterogeneous material, and this can be attributed to the variety of OM sources and
981 the different decomposition processes favoured by the variety of environments in which OM is found. In
982 this study we are using the same type of OM for both types of sorption, therefore we can use C
983 functionalities commonly found in OM to qualify the presence of OC sorption; amides, carboxylic acids,
984 and aromatics, which signify the presence of proteins, polysaccharides, and terrestrial OM, respectively.
985 These images show substantial co-localization between the Fe(II) from FeS and the carbon from
986 planktonic OM. Out of the three types of functionalities, carboxylic C (at 288.6 eV) shows the highest
987 presence for both adsorption and co-precipitation, not an unexpected result considering that carboxylic-

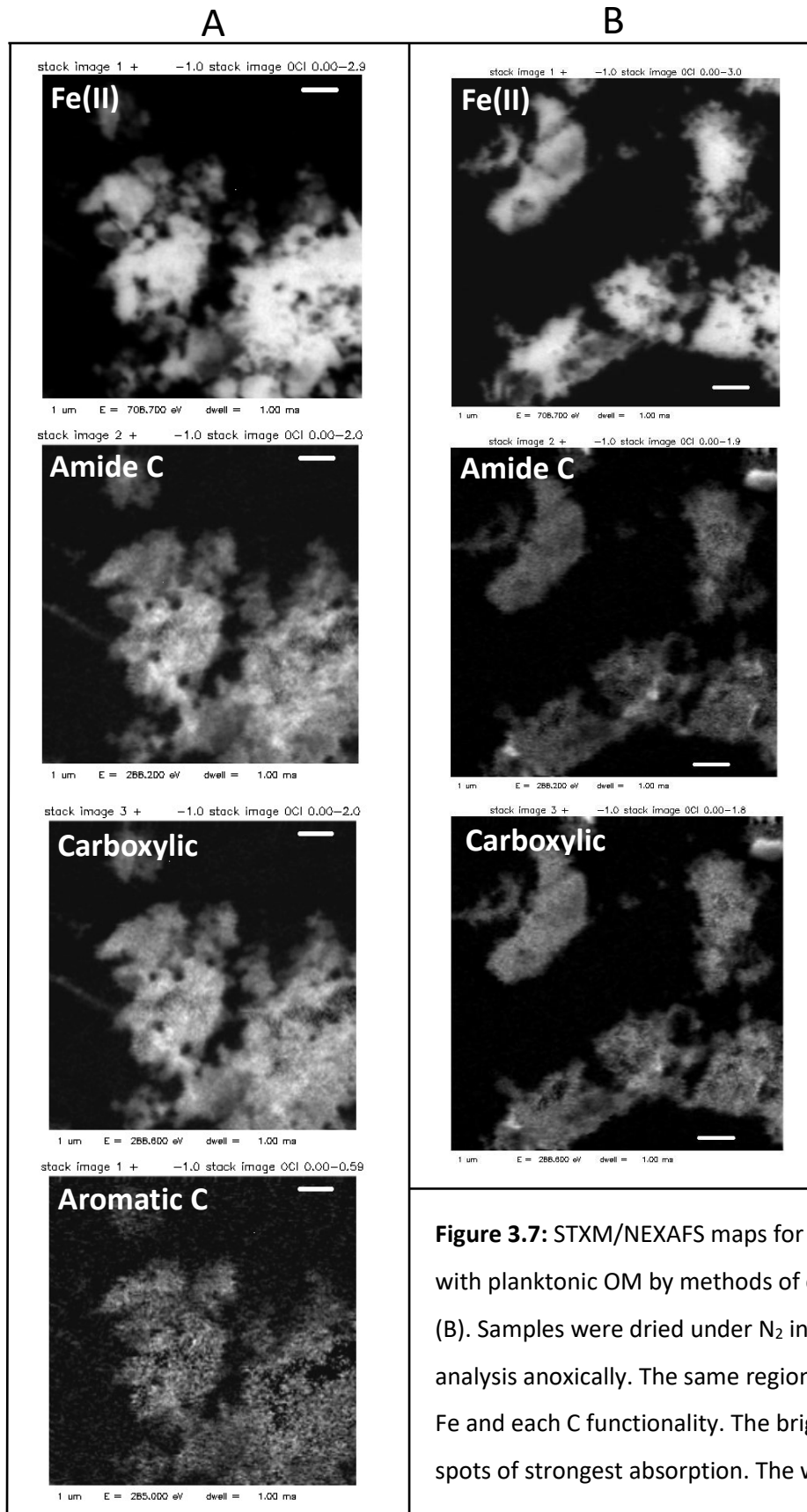


Figure 3.7: STXM/NEXAFS maps for the synthetically prepared FeS with planktonic OM by methods of co-precipitation (A) and adsorption (B). Samples were dried under N₂ in the glove box and transported for analysis anoxically. The same region on the particle was examined for Fe and each C functionality. The brightest regions on the images are spots of strongest absorption. The white bar represents 1 μm.

rich molecules are a major constituent of refractory marine dissolved OM (149). The map for aromatic C (at 285 eV) is absent in the second column because the concentration of aromatic C was not significant, largely due to the lack of OM from a terrestrial origin, which would provide aromatic-containing macromolecules such as lignin and tannin and their degradation products (150). In contrast, x-ray absorption for the amide C functionality (at 288.2 eV), which represents protein and chitin (151), was strong for both adsorption and co-precipitation. Overall, FeS co-precipitated with OM showed more OM in the sample than when FeS precipitated and then OM was added.

Qualitatively, the images show some inter- and intra-particle heterogeneity, but not to the extent that is seen in natural samples, this is expected for a controlled system like this one. There are sections of higher concentration for each energy (especially seen in the STXM maps for the amide C) in the imaged particle, but the distribution of Fe(II) is consistent throughout the parts that are illuminated, with only minimal fading on the edges (possibly due to surficial oxidation). It might be expected to see C functionalities only on the perimeters of the particle aggregates for the adsorption precipitates, but what we see is the C functionalities interspersed throughout the particle, like the co-precipitates. This may be due to the small scale of the STXM maps or the sample preparation.

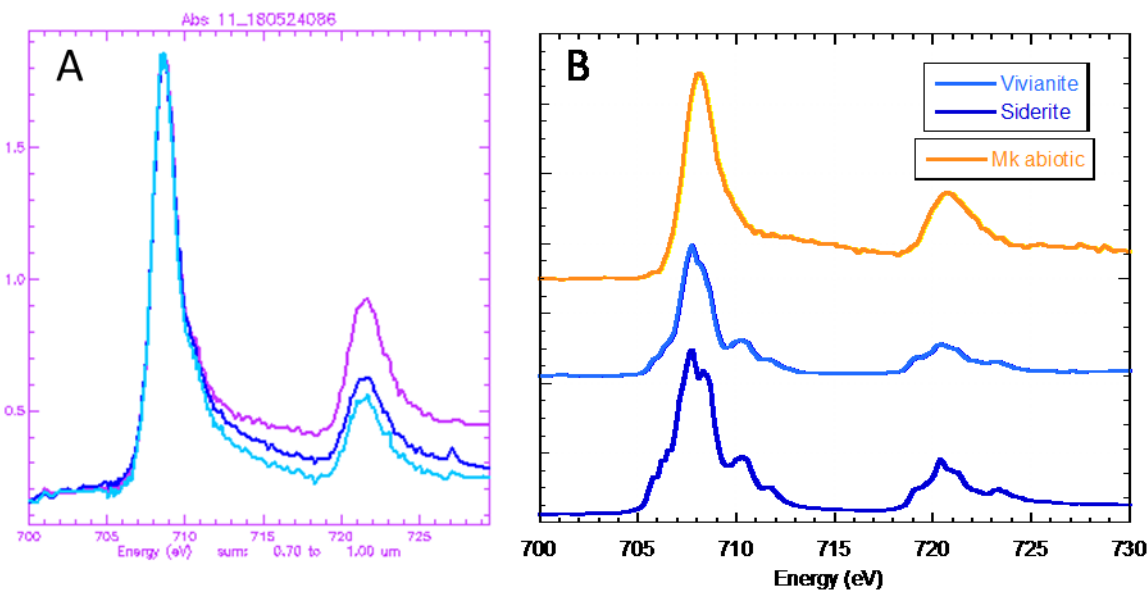


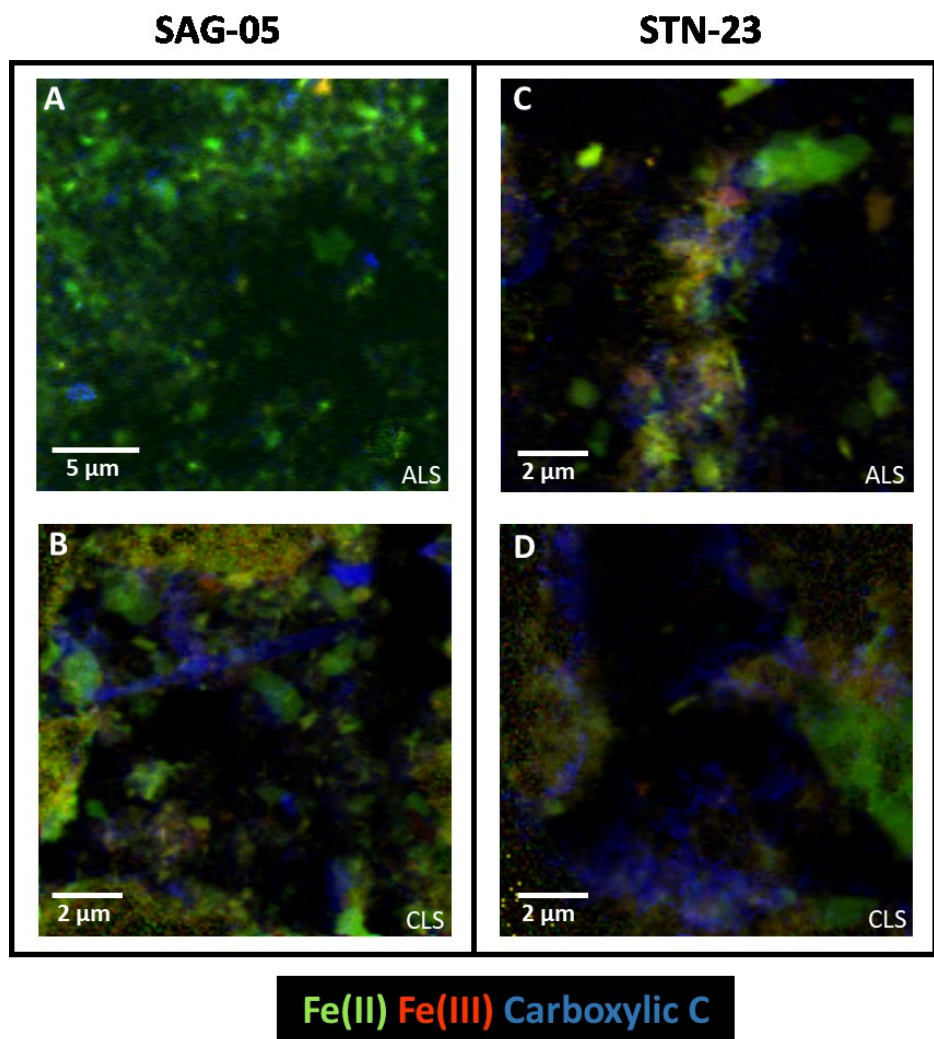
Figure 3.8: The NEXAFS spectrum of the Fe L_{III} -edge of synthetic FeS co-precipitated with NOM (A), compared to the spectra of the reference compounds (B); Mackinawite (FeS), Vivianite ($\text{Fe}^{2+}\text{Fe}_2^{2+}(\text{PO}_4)_2\cdot 8\text{H}_2\text{O}$), and Siderite (FeCO_3), which are all commonly found in sediments and contain Fe^{2+} .

1004 **3.5.2 Anoxic Sediment Samples**

1005 Along with the synthetic FeS, XANES and STXM/NEXAFS was carried out on anoxic sediment samples
1006 from SAG-05 and STN-23 that were dried under N₂ in the glove box and shipped for analysis in O₂-free
1007 conditions. The most abundant C functional group was that of carboxylic acid at 288.6 eV, and thus was
1008 used for these scans. The resulting elemental maps (Figure 3.9) show varying extents of co-localization
1009 between Fe(II), Fe(III), and the carboxylic acid functionality of OM at these two sampling stations. One
1010 downside of STXM/NEXAFS analysis is that it is difficult to draw quantitative conclusions, especially
1011 when working with a complex natural sample. In this case, both stations showed the presence of Fe(II),
1012 possibly from FeS, or other Fe(II) bearing minerals such as siderite or vivianite, and Fe(III), possibly from
1013 Fe-oxides.

1014

Figure 3.9: STXM/NEXAFS maps for anoxic sediment from two stations, SAG-05 (A,B) and STN-23 (C,D) showing distribution of ferrous iron, ferric iron, and carboxylic C in the sample. Images on the top row (A,C) were obtained at the American Light Source (ALS) in California, USA, and images on the bottom row (B,D) were obtained at the Canadian Light Source (CLS) in Saskatchewan, Canada.



1015

1016 In the image obtained at the ALS from sediment at Station SAG-05, we see mostly areas of green, with a
1017 few scattered areas of intense purple; these colours express the co-localization of Fe(II) with carboxylic
1018 C, and Fe(III) with carboxylic C, respectively. The sediment at this site was at an anoxic depth and
1019 contained high levels of AVS (observed as well as measured), about 10-fold more than at STN-23,
1020 therefore it is expected to see Fe(II) to this extent. At the resolution provided in this STXM image, Fe(II)
1021 in this sample (although not confirmed to be purely FeS) appears to be exclusively co-localized to
1022 carboxylic C. Although this is an anoxic sediment, some Fe(III) has resisted reductive dissolution and
1023 appears co-localized with carboxylic C, appearing as additional evidence for Fe-oxide promoted OC
1024 preservation (48, 130). An interesting result is that in this image the C fraction is not observed separately
1025 from Fe(II) and Fe(III), and that Fe(II) and Fe(III) appear to exist interspersed with each other, but as
1026 isolated phases. The images obtained at the CLS for sediment from SAG-05 show areas of carboxylic C
1027 that is not co-localized to Fe(II) or Fe(III), but also not localized to the surface of the aggregates. Overall
1028 at SAG-05 we see a small amount of carboxylic C and Fe(III) co-localization, some independent species,
1029 and significant Fe(II) and carboxylic C co-localization.

1030 The sediment samples from STN-23 tell a different story; here we see co-localization of the three
1031 species, as well as separate presence. In the images for STN-23 taken at the ALS, aggregates of the three
1032 species are apparent, with independent green areas interspersed around the image. These separate
1033 green areas appear to be similar to the green areas seen in the sediment from SAG-05. Overall
1034 compared to SAG-05, this sample presents fewer purple areas (Fe(III) co-localized with carboxylic C),
1035 instead demonstrating distinct areas of Fe(III) and carboxylic C. The blue areas appear to be present
1036 mainly on the outside of the aggregates (especially for the images from the CLS) and intermingled in
1037 their innards. Areas of co-localization of Fe(II) and carboxylic C reside in the aggregates, but do not exist
1038 homogeneously, as seen in the particles imaged at the CLS at STN-23.

1039 **4 Discussion**

1040 **4.1 Sorption Between NOM and FeS**

1041 Profiles of sediment show the concentration of certain species in the solid- and liquid-phase from the
1042 sediment-water interface to depth of the sediment core (Figures 3.1 and 3.2). Sediment data from the
1043 two sampling stations used in this study in 2017 shows removal of Fe from the liquid phase (moving into
1044 the solid-phase as mackinawite, FeS_m) correlating with the stabilization of DOC at a similar depth. The
1045 sulfide profiles show concentrations in the pore water that are below the detection limits until about 35

1046 cm. At this point we observe a sudden increase of the sulfide concentration, for example at SAG-05
1047 (Figure 3.1), to a level of about 75 µM, corresponding to a dissolved Fe(II) concentration of 13 µM and a
1048 dissolved Fe(III) concentration of 9 µM. It is at this depth where finally the concentration of sulfide
1049 exceeds that of ferrous iron in the pore water. An increase in AVS at this depth (33.5 cm) (ie.
1050 precipitation of FeS_m) is observed but does not completely remove the ferrous iron from the aqueous-
1051 phase as one may expect. This iron may be stabilized by other species in the matrix or FeS_{aq} , in the
1052 liquid-phase, is contributing to the measurements of dissolved iron and sulfide in the pore water. The
1053 lack of precipitation of FeS_m may be due to the decrease of pH in the sediment, due to previous FeS_m
1054 precipitation (which liberates a proton). Previous research at this location showed almost complete
1055 removal of dissolved iron at depth at SAG-05 corresponding to a high concentration of AVS and a high
1056 concentration of OC in the solid phase (111). If we are in fact seeing FeS_m -promoted DOC-sorption or co-
1057 precipitation (thus suggesting preservation) in a complex matrix like the one found in sediment, we can
1058 expect to find Fe and OC co-localized in anoxic sediment samples from STN-23 and SAG-05.

1059 STXM/NEXAFS can show spatial co-localization of specific atoms and has been used for complex natural
1060 samples such as soils (26, 135–137) and sediments (48, 132). The STXM/NEXAFS done for this study on
1061 sediment from SAG-05 and STN-23 shows co-localization at both stations (Figure 3.9). SAG-05 shows
1062 carboxylic C incorporated into the Fe-structures and on the surface, and STN-23 shows mainly carboxylic
1063 C on the surface. This may be presenting different types of sorption, depending on the chemical
1064 environments. Carboxylic C is used as a signifier of acidic polysaccharide-rich OM (136) which has been
1065 characterized as fresh OM that is aquagenic – OM from a marine source (53). The sediment used for
1066 STXM-NEXAFS imaging was taken from depth (>35 cm), therefore finding “fresh” OM on the surface of
1067 the Fe-containing particles shows a potential protective interaction. The difference in appearance and
1068 composition of the two anoxic sediments can be attributed to the varying depositional and chemical
1069 environments, for example the $\text{Fe(II)}:\text{S}^{2-}$ ratio, the pH of the pore water, or the concentration and
1070 molecular content of present OM at the time of precipitation. A limitation of STXM/NEXAFS imaging of
1071 complex natural samples is that it is time and resource-demanding and only targets small physical areas
1072 in a sample. This restraint is apparent in the attempt to draw conclusions from these images; the images
1073 from STN-23 samples could be showing evidence of adsorption; FeS formed before exposure to NOM
1074 which is why carboxylic C is mainly present on the particle surfaces, but with images from only two areas
1075 of approximately 0.01 mm x 0.01 mm, evidence supporting this conclusion is fragile.

1076 Another limitation of our sediment images is that only one functional group for OC was probed (that of
1077 carboxylic C, due to the strong signal), and this was used as a total representation of OM in the
1078 sediment. The images of the synthetically precipitated FeS with DOM by co-precipitation and adsorption
1079 (Figure 3.7), besides showing clear evidence of an FeS-mediated interaction, give more information
1080 about which functional groups of OC may be preferentially sorbed. The preferred functions groups for
1081 our precipitated FeS are, from highest to lowest affinity: carboxylic C, amide C, and aromatic C (not
1082 enough signal in the case of adsorption). This difference in affinity may be a consequence of the
1083 functional groups available for sorption or it may be a clue into the type of binding that is taking place
1084 between OC and FeS. In the case of iron oxides, synthesized ferrihydrite co-precipitated with different
1085 types of OM showed that the OM the most incorporated into the aggregate was the one with the
1086 highest amount of carboxyl C (59). The carboxylic C functional group has been seen co-localized to Fe
1087 oxides in a variety of studies, an interaction that has been shown as of inner-sphere type (152). Despite
1088 the STXM evidence in this study showing that FeS and carboxylic C functionalities are co-localized, we
1089 cannot assume that this is due to an inner-sphere interaction like that of Fe oxides; additional work
1090 would be needed to confirm the type of interactions between FeS and OM.

1091 There are a couple downsides to synchrotron analysis with heterogeneous material: many
1092 measurements are required to get an accurate understanding of the microscopic distributions within the
1093 heterogeneous sample and the resulting spectra is complex and hard to interpret which limits
1094 quantitative ability. The synthetic FeS experiments provide an environment that can be simplified and
1095 the parameters, controlled. The STXM/NEXAFS images show substantial co-localization between NOM
1096 and FeS for both types of sorption, but in order to ascertain information about different affinities per
1097 source of OM from natural environments, sorption isotherms were built using plankton, soil, and corn
1098 NOM. These sources of NOM were chosen as a representation of marine and terrestrial ("old" and
1099 "fresh") OM, respectively. The molecular make-up of these NOM solutions was not characterized; NOM
1100 is notoriously hard to characterize on a molecular level due to the complexity and heterogeneity of the
1101 mixture (153). Despite the fact that the molecular composition of the NOM used in this study is not
1102 known, several reasonable assumptions can be stated: the planktonic and corn OM are less aged than
1103 the soil OM and can be expected to contain larger molecules of higher reactivity; the soil and corn OM
1104 (terrigenous) contain molecules of a lignin and cellulose origin, at various levels of decomposition (67);
1105 and the planktonic OM (aquagenic) contains the highest abundance of polysaccharides (carboxylic C)
1106 and peptides (amide C) relative to corn and soil OM (53). Isotherms allow a better understanding the

1107 FeS-OM interactions by visually demonstrating for which OM FeS has a higher initial affinity and a
1108 greater sorption capacity.

1109 The experimentally obtained isotherms shown in Figure 3.3 compare the two sorption types and NOM
1110 from the three sources. As expected, co-precipitation resulted in a higher sorption capacity than
1111 adsorption for all three NOM types, simply because in adsorption, OM can potentially interact with FeS
1112 molecules at the surface of the solid while for co-precipitation, these interactions are taking place as the
1113 solid forms, thus a higher proportion of the FeS molecules are exposed and can interact with the OM.
1114 The adsorption isotherms showed the highest sorption capacities for plankton above corn, and lastly soil
1115 OM. Fitting isotherm models to the experimental data allows for quantitative comparison not only in
1116 this experiment but to other studies as well. The Langmuir isotherm model is perhaps the most widely
1117 used for adsorption modelling, but it cannot be used without acknowledging the intrinsic assumptions.
1118 The Langmuir model assumes that the adsorbate is sorbed as a monolayer onto the adsorbent, each
1119 binding site on the adsorbent has the same affinity for the adsorbate, and that interactions between the
1120 adsorbate molecules is absent (154). The Freundlich isotherm model allows for more freedom;
1121 describing a heterogeneous system with decreasing attraction of the adsorbate to the adsorbent,
1122 sorption that is not limited to a monolayer (non-uniform), that is non-ideal and reversible. Theoretically
1123 from this model, the binding sites with the strongest affinity are occupied first, resulting in a decreasing
1124 adsorption energy throughout the sorption process. The isotherm model that best fits our experimental
1125 data (judged by the smallest error function values in Tables 3.2 and 3.3) is that of Redlich-Peterson. This
1126 is a notably versatile model that tries to describe sorption over a large range of adsorbate
1127 concentrations; at low concentration it tends towards the Langmuir model and at high concentration it
1128 tends towards the Freundlich model. However, the closeness of the fit of the Redlich-Peterson model
1129 may be due to over-parameterization; two of its parameters are un-interpretable, so in this case, a
1130 better fit does not necessarily give more information.

1131 The multitude of chemical species present in natural systems means that the precipitation of FeS from
1132 dissolved ferrous iron and sulfide is highly unlikely to occur as an isolated event. More likely, FeS co-
1133 precipitates in the presence of organic ligands and ions (precipitation is on the scale of milli-seconds (5)),
1134 and then this aggregate adsorbs other species. Indeed, if co-precipitation was as slow as the sorption
1135 onto the FeS surface, we would see a linear relationship on our experimental isotherms as OM is
1136 continuously incorporated into the co-precipitate. Instead we see a high initial affinity followed by a
1137 plateau for the co-precipitation runs, like the adsorption isotherms. OM was first thought to sorb

1138 mineral surfaces as a monolayer (46, 47) but this hypothesis has been largely disproven; it is now known
1139 that OM sorbs onto sediment minerals rather in discontinuous “blebs” or “smears” (155), specifically at
1140 the particle edges (156). The difficulty with using models for the sorption of NOM is that the
1141 heterogeneity of the mixture and the probability of large molecules means that the negative charges on
1142 NOM that are partly sorbed onto mineral surfaces interact and repel each other, decreasing the affinity
1143 of the surface for more NOM sorption (66), but to an extent that is immeasurable.

1144 A study using NOM from a wetland pond sorbed onto Fe oxides (66) found K_L values for the Langmuir
1145 isotherm that are lower than the values obtained in this study by 1-2 order of magnitude. Regardless,
1146 the isotherms presented in this study show that there certainly is a sorptive interaction between FeS
1147 and NOM, and that the interaction occurs preferentially with NOM originating from plankton. This may
1148 mean that this type of OM contains the highest relative abundance of carboxylic C functional groups,
1149 and this may give hints to the type of interaction taking place (discussed further in Section 4.4). The
1150 STXM/NEXAFS images show that in both synthetic and sediment samples FeS and OC functionalities are
1151 co-localized. What this means for the behaviour and character of the FeS-OM moieties is explored the
1152 sections below.

1153 4.2 The Effect of OM on FeS Aggregation

1154 In natural systems, FeS precipitates in the presence of many other complexes and ions, which
1155 undoubtably has an effect on its aggregation characteristics. OM is ubiquitous in sediment; in this
1156 system it is the electron source for sulfate-reducing bacteria (SRB) which produce the sulfide, even so,
1157 its interactions with FeS have been scarcely explored. A study done in 2018 by Picard *et al.* used TEM
1158 and SEM imaging to show that the presence of SRB influences the physical characteristics of FeS; larger
1159 aggregates form with a different surface texture, FeS uses the SRB as nucleation sites, and the presence
1160 of live SRB increases the rate of transformation of FeS to Fe_3S_4 (107). In agreement with Picard’s work,
1161 our SEM results show that NOM from lysed plankton when co-precipitated with FeS increases the size of
1162 the FeS particles, and alters the surface texture (Figure 3.5), which may have an effect on the isotherm
1163 results. If the FeS particles are smaller when precipitated before exposure to NOM than when co-
1164 precipitated with NOM, this will affect the isotherm sorption capacities; leading to an increase in the
1165 amount of NOM sorbed through adsorption just as a consequence of an increased surface area. One
1166 reason for the larger FeS aggregates in the presence of OM could be due to a mechanism named the
1167 “onion hypothesis” (157); through the direct interaction of some of their functional groups with FeS
1168 particles, the OM molecules act as the adhesive between successively added layers of FeS particles, thus

1169 increasing the overall size of the aggregates. This mechanism has been demonstrated for iron oxides
1170 with natural riverine OM (157). TEM data has also shown that the overall cohesion of natural sediment
1171 is promoted by OM increasing aggregation (155).

1172 This work and the one done by Picard *et al.* (2018) are the only studies available in literature reporting
1173 OM's effect on FeS aggregation. This pales in comparison to the research on OM interactions with Fe(III)
1174 oxides in terms of their collective stability and aggregation characteristics. One study found similar
1175 results for Fe oxide nanoparticles to what we found for FeS; that the presence of NOM during
1176 precipitation results in larger aggregates (158). The presence of bacterial cells has also been shown to
1177 change the spatial organization of Fe oxides (159). As mentioned earlier, this is not a one sided
1178 relationship; the interaction between the Fe oxide and OM affects both parties; OC in aggregates is
1179 protected from mineralization and also no longer participates in diffusion (44). One study used STXM to
1180 find that OM quality in soil was different depending its location: OM outside of the mineral aggregate
1181 was more "processed", and had more carbonyl-C relative to aromatic-C, indicating surficial oxidation
1182 (135). Colloids of Fe oxides and OM have been found to be stabilized due to repulsive and electrostatic
1183 forces (160) which depend on the pH and OM concentration in solution (161).

1184 **4.3 The Effect of NOM on FeS Reactivity Towards O₂**

1185 OM is known to act as a ligand to metal complexes in natural environments, but whether it contributes
1186 to stabilize or destabilize these complexes has been up for debate (162). In the aqueous phase, Fe(II)
1187 binding to OM in oxic water is protected against oxidation (163). In the solid-phase, NOM protects Fe
1188 oxides such as lepidocrocite from reductive dissolution due to OM and other anions forming inner-
1189 sphere complexes that compete with a reducing agent, such as dissolved sulfide or ferrous iron (164).
1190 Elemental sulfur has also been shown to be protected from microbial oxidation by dissolved organic
1191 molecules originating from marine or terrestrial OM (165). FeS is oxidized by O₂ as per the following
1192 reaction (166):



1194 Our SEM results suggest that FeS-OM aggregates would be more resistant to oxidation owing to the
1195 larger particle size and lower surface area. In addition, the highly-textured surface of the larger co-
1196 precipitated particles compared to the smaller and smooth OM-free FeS particles also suggests that
1197 their surface would be less reactive as it is very likely that the functional groups of the co-
1198 precipitated OM present at the surface would get oxidized to moieties such as hydroxyls and carboxyls,

which are less interesting for biological degradation as their energy yield upon oxidation is lower than for more reduced moieties. Although speculative at this point, one could envision co-precipitated FeS-OM aggregates with the majority of the OM embedded within the particles and protected by their FeS coatings or shell, with the surface of the FeS-OM aggregates covered with partly oxidized OM moieties covering the exterior of the shell and thus protecting the surface FeS molecules from oxidation. This hypothesis seems supported by the data shown in Figure 3.6, where protection of FeS from oxidation is apparent at high concentrations of co-precipitated OM. More work is obviously needed to confirm this hypothesis. Importantly, oxidation of FeS at the surface of the aggregates would lead to the formation of Fe(III) oxides, which have also been shown to be very effective in protecting OM from degradation.

4.4 Surface Chemistry of FeS and NOM

Although the data obtained in this study cannot directly confirm whether FeS and NOM are interacting on the inner- or outer-sphere level, the conclusion that there is in fact some sorption occurring opens up the query of the nature of the interaction. Iron oxides are known to interact with OM on through both types of interactions. The electrostatic interaction is due to the surface charges on the oxide and the negative charge on the OM (carboxylic acids in particular, which are very abundant in natural OM, have pK_a values that are much lower than that of seawater and pore water and are thus deprotonated). The “zero-point charge” (pH_{ZPC}) is a value that defines the pH above which the complex’s surface is negatively charged, and below which the complex is positively charged. The pH_{ZPC} of Fe oxides are as follows: ferrihydrite 7.8-7.9, lepidocrocite 6.7-7.3, hematite 7.5-9.5, and goethite 7.5-9.5 (6), but depends on the mode of preparation. One study found a pH_{ZPC} for their synthesized goethite to be 9.2 (63), meaning that the interactions between OM and Fe oxides only occur (electrochemically) below pH 9.2 until the pH is reached where the OM becomes positively charged. There is a smaller pH range for FeS-OM outer-sphere interactions than for goethite; because the pH_{ZPC} for FeS_m has been found to be 7.5 (96). However, because the pH of pore waters is generally slightly below this pH owing to the production of carbonic acid upon the oxic degradation of organic carbon and small organic acids under O₂-free conditions (fermentation), as well as the liberation of protons upon the precipitation of iron hydroxides near the sediment-water interface, the surface of the FeS nanoparticles formed upon nucleation bear a positive charge that is highly favorable for establishing electrostatic interactions with the negatively charged natural dissolved OM, which could eventually lead to the kinetically slower formation of inner-sphere covalent bonds between iron and the organic molecules.

1229 **5 Conclusions and Future Work**

1230 The work presented here demonstrates that there is an interaction between organic compounds in
1231 NOM and FeS synthesized in our lab under conditions that mimic the natural environment in which they
1232 form in sediments. Although more characterization is needed, the sampling station SAG-05 represents
1233 an ideal location for exploring naturally-occurring iron sulfide minerals and OM largely because of the
1234 geographical location of the site and its biogeochemical characteristics. At this Saguenay Fjord sampling
1235 site, where the bottom water salinity is around 30 salinity units (close to that of open oceanic water at
1236 about 35), the OM is of largely terrigenous origin (167) and O₂ is depleted in first few millimeters below
1237 the sediment-water interface due to large bacterial oxygen demand during OM degradation and the
1238 oxidation of reduced inorganic compounds (112). Anoxic sediment from this site was imaged using
1239 STXM/NEXAFS and tight Fe(II)-OM co-localization was found. The results from these field samples was
1240 corroborated with synthetic sorption experiments that showed preferential sorption of more labile
1241 planktonic OM over soil and corn OM. This means that the OM protection mechanism by FeS, quenching
1242 or greatly reducing the kinetics of OM microbial degradation, would have the highest contribution in
1243 transition zones such as coastal and estuarine environments where there is a large input of marine OM
1244 derived from the increased primary productivity stimulated by the high inputs of nutrients from the
1245 riverine discharge, combined with an equally large discharge of terrestrial organic matter, leading to the
1246 accumulation of organic-rich and iron-rich sediments under anoxic conditions. These characteristics are
1247 highly favorable to the formation of FeS-OM aggregates, compared to marine environments where the
1248 flux of OM and iron to the sediment is lower.

1249 It is currently impossible to quantify the importance of this protection mechanism in the global
1250 preservation or organic carbon in marine sediments because the size of the global sedimentary FeS
1251 pools has never been estimated. However, even if we assume that only about half of the sedimentary
1252 OC carbon pool is preserved through its interactions with iron oxides (estimated at 19 to 45 x 10¹⁵ grams
1253 of OC, or about 21% of the global sedimentary OC inventory in the world ocean (130)), OM sorption
1254 onto or co-precipitation within FeS particles could lead to the protection of a significant fraction of
1255 sedimentary OC, in the range of 10 to 20 x 10¹⁵ grams of OC. We acknowledge that the size of this pool is
1256 still speculative at this point, but our study is the first to provide a starting point and research template
1257 to refine this estimate.

1258 By comparison to iron sulfides' sedimentary neighbour (Fe oxides), the interactions of FeS with OM have
1259 been scarcely studied and characterized; however FeS has been receiving attention for its properties as

1260 a sorptive material for toxic metals such as mercury and arsenic (104, 105). The work presented in this
1261 thesis is the first study to perform sorption isotherms on FeS and NOM with the intention to quantify
1262 the interaction through sorption characteristics, especially for comparison with Fe oxides. Although we
1263 found lower sorption affinity and capacity of our FeS particle than has been found for Fe oxides by way
1264 of the Langmuir isotherm model (66), our findings prove that there is a strong sorptive interaction
1265 whose extent and consequences for the global carbon cycle have yet to be characterized. Pyrite (FeS_2),
1266 for which FeS is often called the precursor, has been found to have OM incorporated into the structures
1267 as biofilm (168) and is often found in close association with the most refractory fraction of sedimentary
1268 OM which survives degradation once the more labile compounds are completely degraded. FeS could
1269 act as a transporter of OM through its sorptive protection, stabilizing OM in anoxic sediments until FeS
1270 dissolves, releasing OM, and FeS_2 forms (102). Pyrite has been found in some of the oldest sedimentary
1271 rocks (3.8×10^9 yr old) (8), and has been correlated to OC content in sediments (169). Thus, if pyrite is
1272 incorporating this OM from FeS into its structure or is involved in a sorption interaction with OM, the
1273 OM from FeS could remain stable for a very long time.

1274 To further the characterization of FeS-OM sorption in terms of the effect on preserving OM from
1275 microbial degradation, protecting FeS from oxidation, and changing the aggregation characteristics of
1276 the particles, more experiments are needed. To expand on our SEM results showing an increase of
1277 particle size with OM, characterization of the surface area should be done using a Brunauer–Emmett–
1278 Teller (BET) instrument. Preliminary measurements were attempted recently but showed a suspiciously
1279 low surface area of a few square meters per gram given the physical characteristics of FeS particles. The
1280 size of FeS aggregates when precipitated without OM compared to in the presence of OM can be further
1281 explored using a Dynamic Light Scattering device to corroborate the BET and SEM measurements and
1282 compare the average particle size of FeS and FeS-OM particles suspended in water rather than freeze-
1283 dried. Finally, the types of interactions can be probed using synchrotron analysis, using a similar
1284 approach as what has recently been done for OM-Fe oxides (48): by looking at the iron K_1 edges using
1285 XANES and EXAFS to probe the local molecular environment of the central iron atom, it is theoretically
1286 possible to probe whether the interaction with organic carbon is of the inner- or outer-sphere can be
1287 known if the interaction is inner- or outer-sphere type. The type of interaction has broad implications for
1288 the fate of both FeS and OM in terms of its diagenetic pathway in sediment.

References

1. O. P. Mehra, Iron Oxide Removal from Soils and Clays by a Dithionite-Citrate System Buffered with Sodium Bicarbonate. *Clays Clay Miner.* **7**, 317–327 (1958).
2. A. Mucci, M. Starr, D. Gilbert, B. Sundby, Acidification of Lower St. Lawrence Estuary Bottom Waters. *Atmosphere-Ocean.* **49**, 206–218 (2011).
3. J. I. Hedges, R. G. Keil, Sedimentary organic matter preservation: an assessment and speculative synthesis. *Mar. Chem.* **49**, 81–115 (1995).
4. E. A. Canuel, S. S. Cammer, H. A. McIntosh, C. R. Pondell, Climate Change Impacts on the Organic Carbon Cycle at the Land-Ocean Interface. *Annu. Rev. Earth Planet. Sci.* **40**, 685–711 (2012).
5. D. Rickard, G. W. Luther, Chemistry of Iron Sulfides. *Chem. Rev.* **107**, 514–562 (2007).
6. R. M. Cornell, U. Schwertmann, *The Iron Oxides: Structure, Properties, Reactions, Occurrences and Uses* (Wiley, 2006; <https://books.google.ca/books?id=CCnNKzh4oKUC>).
7. S. W. Poulton, M. D. Krom, R. Raiswell, A revised scheme for the reactivity of iron (oxyhydr)oxide minerals towards dissolved sulfide. *Geochim. Cosmochim. Acta.* **68**, 3703–3715 (2004).
8. D. Rickard, *Sulfidic Sediments and Sedimentary Rocks* (Elsevier Science, 2012), *Developments in Sedimentology*.
9. J. G. Canadell *et al.*, Contributions to accelerating atmospheric CO₂ growth from economic activity, carbon intensity, and efficiency of natural sinks. *Proc. Natl. Acad. Sci.* **104**, 18866–18870 (2007).
10. S. CO₂.Earth, Daily CO₂. *CO2.Earth* (2019), (available at <https://www.co2.earth/daily-co2>).
11. J. M. Guinotte, V. J. Fabry, Ocean acidification and its potential effects on marine ecosystems. *Ann. N. Y. Acad. Sci.* **1134**, 320–342 (2008).
12. M. L. Bender, D. T. Heggie, Fate of organic carbon reaching the deep sea floor: a status report. *Geochim. Cosmochim. Acta.* **48**, 977–986 (1984).
13. D. J. Burdige, Burial of terrestrial organic matter in marine sediments: A re-assessment. *Glob. Biogeochem. Cycles.* **19** (2005), doi:10.1029/2004GB002368.
14. D. Hammond, in *Encyclopedia of Ocean Sciences (Second Edition)*, J. H. Steele, Ed. (Academic Press, Oxford, 2001; <http://www.sciencedirect.com/science/article/pii/B9780123744739001818>), pp. 563–571.
15. T. D. Jickells *et al.*, Global Iron Connections Between Desert Dust, Ocean Biogeochemistry, and Climate. *Science.* **308**, 67–71 (2005).
16. S. W. Poulton, R. Raiswell, The low-temperature geochemical cycle of iron: From continental fluxes to marine sediment deposition. *Am. J. Sci.* **302**, 774–805 (2002).

17. R. Raiswell, D. E. Canfield, Sources of iron for pyrite formation in marine sediments. *Am. J. Sci.* **298**, 219–245 (1998).
18. F. J. Millero, Solubility of Fe(III) in seawater. *Earth Planet. Sci. Lett.* **154**, 323–329 (1998).
19. E. J. P. Phillips, D. R. Lovley, E. E. Roden, Composition of Non-Microbially Reducible Fe(III) in Aquatic Sediments. *Appl Env. Microbiol.* **59**, 2727–2729 (1993).
20. D. R. Lovley, E. J. P. Phillips, Organic Matter Mineralization with Reduction of Ferric Iron in Anaerobic Sediments. *Appl Env. Microbiol.* **51**, 683–689 (1986).
21. K. Kuma, J. Nishioka, K. Matsunaga, Controls on iron(III) hydroxide solubility in seawater: The influence of pH and natural organic chelators. *Limnol. Oceanogr.* **41**, 396–407 (1996).
22. F. J. Millero, W. Yao, J. Aicher, The speciation of Fe(II) and Fe(III) in natural waters. *Mar. Chem.* **50**, 21–39 (1995).
23. M. Sandy, A. Butler, Microbial Iron Acquisition: Marine and Terrestrial Siderophores. *Chem. Rev.* **109**, 4580–4595 (2009).
24. M. Miethke, M. A. Marahiel, Siderophore-Based Iron Acquisition and Pathogen Control. *Microbiol. Mol. Biol. Rev. MMBR.* **71**, 413–451 (2007).
25. R. G. Pearson, Hard and soft acids and bases, HSAB, part II: Underlying theories. *J. Chem. Educ.* **45**, 643 (1968).
26. M. Schumacher, I. Christl, A. C. Scheinost, C. Jacobsen, R. Kretzschmar, Chemical Heterogeneity of Organic Soil Colloids Investigated by Scanning Transmission X-ray Microscopy and C-1s NEXAFS Microspectroscopy. *Environ. Sci. Technol.* **39**, 9094–9100 (2005).
27. B. L. Lewis *et al.*, Voltammetric estimation of iron(III) thermodynamic stability constants for catecholate siderophores isolated from marine bacteria and cyanobacteria. *Chem. Iron Seawater Its Interact. Phytoplankton.* **50**, 179–188 (1995).
28. E. L. Rue, K. W. Bruland, Complexation of iron(III) by natural organic ligands in the Central North Pacific as determined by a new competitive ligand equilibration/adsorptive cathodic stripping voltammetric method. *Mar. Chem.* **50**, 117–138 (1995).
29. W.-J. Cai, F. L. Sayles, Oxygen penetration depths and fluxes in marine sediments. *Mar. Chem.* **52**, 123–131 (1996).
30. N. N. Rabalais, in *Encyclopedia of Ocean Sciences (Second Edition)*, J. H. Steele, Ed. (Academic Press, Oxford, 2009; <http://www.sciencedirect.com/science/article/pii/B9780123744739006469>), pp. 172–180.
31. D. Gilbert, B. Sundby, C. Gobeil, A. Mucci, G.-H. Tremblay, A seventy-two-year record of diminishing deep-water oxygen in the St. Lawrence estuary: The northwest Atlantic connection. *Limnol. Oceanogr.* **50**, 1654–1666 (2005).

32. Q. H. Tran, G. Unden, Changes in the proton potential and the cellular energetics of *Escherichia coli* during growth by aerobic and anaerobic respiration or by fermentation. *Eur. J. Biochem.* **251**, 538–543 (1998).
33. I. Koike, J. Sorensen, Nitrate reduction and denitrification in marine sediments. *Nitrogen Cycl. Coast. Mar. Environ.*, 251–273 (1988).
34. J. E. Post, Manganese oxide minerals: Crystal structures and economic and environmental significance. *Proc. Natl. Acad. Sci.* **96**, 3447–3454 (1999).
35. V. E. Oldham, M. T. Miller, L. T. Jensen, G. W. Luther III, Revisiting Mn and Fe removal in humic rich estuaries. *Geochim. Cosmochim. Acta*. **209**, 267–283 (2017).
36. M. Fakhraee, J. Li, S. Katsev, Significant role of organic sulfur in supporting sedimentary sulfate reduction in low-sulfate environments. *Geochim. Cosmochim. Acta*. **213**, 502–516 (2017).
37. J. W. Deming, J. A. Baross, in *Organic Geochemistry: Principles and Applications*, M. H. Engel, S. A. Macko, Eds. (Springer US, Boston, MA, 1993; https://doi.org/10.1007/978-1-4615-2890-6_5), *Topics in Geobiology*, pp. 119–144.
38. J.-A. Bourdoiseau, M. Jeannin, R. Sabot, C. Rémazeilles, P. Refait, Characterisation of mackinawite by Raman spectroscopy: Effects of crystallisation, drying and oxidation. *Corros. Sci.* **50**, 3247–3255 (2008).
39. R. J. Diaz, R. Rosenberg, Marine benthic hypoxia: a review of its ecological effects and the behavioural responses of benthic macrofauna. *Oceanogr. Mar. Biol. Annu. Rev.* **33**, 245–03 (1995).
40. G. Hulthe, S. Hulth, P. O. J. Hall, Effect of oxygen on degradation rate of refractory and labile organic matter in continental margin sediments. *Geochim. Cosmochim. Acta*. **62**, 1319–1328 (1998).
41. T. Komada, C. E. Reimers, G. W. Luther, D. J. Burdige, Factors affecting dissolved organic matter dynamics in mixed-redox to anoxic coastal sediments. *Geochim. Cosmochim. Acta*. **68**, 4099–4111 (2004).
42. H. E. Hartnett, R. G. Keil, J. I. Hedges, A. H. Devol, Influence of oxygen exposure time on organic carbon preservation in continental margin sediments. *Nature*. **391**, 572–575 (1998).
43. J. M. Whittaker, A. Goncharov, S. E. Williams, R. D. Müller, G. Leitchenkov, Global sediment thickness data set updated for the Australian-Antarctic Southern Ocean. *Geochem. Geophys. Geosystems*. **14**, 3297–3305 (2013).
44. T. S. Arnarson, R. G. Keil, Changes in organic matter–mineral interactions for marine sediments with varying oxygen exposure times. *Geochim. Cosmochim. Acta*. **71**, 3545–3556 (2007).
45. J. Six, R. T. Conant, E. A. Paul, K. Paushtian, Stabilization mechanisms of soil organic matter: Implications for C-saturation of soils. *Plant Soil*. **241**, 155–176 (2002).

46. L. M. Mayer, Surface area control of organic carbon accumulation in continental shelf sediments. *Geochim. Cosmochim. Acta.* **58**, 1271–1284 (1994).
47. L. M. Mayer, Relationships between mineral surfaces and organic carbon concentrations in soils and sediments. *Chem. Geol.* **114**, 347–363 (1994).
48. A. Barber *et al.*, Preservation of organic matter in marine sediments by inner-sphere interactions with reactive iron. *Sci. Rep.* **7**, 366 (2017).
49. S. J. Ussher, E. P. Achterberg, P. J. Worsfold, Marine Biogeochemistry of Iron. *Environ. Chem.* **1**, 67–80 (2004).
50. D. Khomskii, *Transition Metal Compounds* (Cambridge University Press, Cambridge, 2014; <http://search.ebscohost.com/login.aspx?direct=true&db=nlebk&AN=878516&site=eds-live>).
51. P. W. Boyd, M. J. Ellwood, The biogeochemical cycle of iron in the ocean. *Nat. Geosci.* **3**, 675–682 (2010).
52. E. D. Melton, E. D. Swanner, S. Behrens, C. Schmidt, A. Kappler, The interplay of microbially mediated and abiotic reactions in the biogeochemical Fe cycle. *Nat. Rev. Microbiol.* **12**, 797–808 (2014).
53. J. W. Gaffney, K. N. White, S. Boult, Oxidation State and Size of Fe Controlled by Organic Matter in Natural Waters. *Environ. Sci. Technol.* **42**, 3575–3581 (2008).
54. C. J. Miles, P. L. Brezonik, Oxygen consumption in humic-colored waters by a photochemical ferrous-ferric catalytic cycle. *Environ. Sci. Technol.* **15**, 1089–1095 (1981).
55. T. L. Theis, P. C. Singer, Complexation of iron (II) by organic matter and its effect on iron (II) oxygenation. *Environ. Sci. Technol.* **8**, 569–573 (1974).
56. J. M. D. Coey, D. W. Schindler, F. Weber, Iron Compounds in Lake Sediments. *Can. J. Earth Sci.* **11**, 1489–1493 (1974).
57. J. E. Kostka, G. W. Luther, Partitioning and speciation of solid phase iron in saltmarsh sediments. *Geochim. Cosmochim. Acta.* **58**, 1701–1710 (1994).
58. U. Schwertmann, Inhibitory Effect of Soil Organic Matter on the Crystallization of Amorphous Ferric Hydroxide. *Nature.* **212**, 645 (1966).
59. C. Mikutta *et al.*, Synthetic coprecipitates of exopolysaccharides and ferrihydrite. Part I: Characterization. *Geochim. Cosmochim. Acta.* **72**, 1111–1127 (2008).
60. U. Schwertmann, F. Wagner, H. Knicker, Ferrihydrite–Humic Associations. *Soil Sci. Soc. Am. J.* **69**, 1009–1015 (2005).
61. R. Cornell, U. Schwertmann, Influence of organic anions on the crystallization of ferrihydrite. *Clays Clay Min.* **27**, 402–410 (1979).

62. T. Akiyama, Microscopic determination of iron-organic aggregates in sea and lake waters. *Geochem. J.* **5**, 39–56 (1971).
63. J. D. Filius, T. Hiemstra, W. H. Van Riemsdijk, Adsorption of Small Weak Organic Acids on Goethite: Modeling of Mechanisms. *J. Colloid Interface Sci.* **195**, 368–380 (1997).
64. Y. Satoh, K. Kikuchi, S. Kinoshita, H. Sasaki, Potential capacity of coprecipitation of dissolved organic carbon (DOC) with iron(III) precipitates. *Limnology.* **7**, 231–235 (2006).
65. R. M. Cornell, P. W. Schindler, Infrared study of the adsorption of hydroxycarboxylic acids on α -FeOOH and amorphous Fe (III)hydroxide. *Colloid Polym. Sci.* **258**, 1171–1175 (1980).
66. B. Gu, J. Schmitt, Z. Chen, L. Liang, J. F. McCarthy, Adsorption and desorption of different organic matter fractions on iron oxide. *Geochim. Cosmochim. Acta.* **59**, 219–229 (1995).
67. K. Kaiser, G. Guggenberger, The role of DOM sorption to mineral surfaces in the preservation of organic matter in soils. *Org. Geochem.* **31**, 711–725 (2000).
68. P. M. Jardine, J. F. McCarthy, N. L. Weber, Mechanisms of Dissolved Organic Carbon Adsorption on Soil. *Soil Sci. Soc. Am. J.* **53**, 1378–1385 (1989).
69. D. M. McKnight *et al.*, Sorption of dissolved organic carbon by hydrous aluminum and iron oxides occurring at the confluence of Deer Creek with the Snake River, Summit County, Colorado. *Environ. Sci. Technol.* **26**, 1388–1396 (1992).
70. S. M. Henrichs, Sedimentary organic matter preservation: an assessment and speculative synthesis—a comment. *Mar. Chem.* **49**, 127–136 (1995).
71. K. Haider, Problems related to the humification processes in soils of temperate climates. *Soil Biochem.* **7**, 55–94 (1992).
72. M. W. Bligh, T. D. Waite, Formation, reactivity, and aging of ferric oxide particles formed from Fe (II) and Fe (III) sources: Implications for iron bioavailability in the marine environment. *Geochim. Cosmochim. Acta.* **75**, 7741–7758 (2011).
73. S. W. Poulton, R. Raiswell, Chemical and physical characteristics of iron oxides in riverine and glacial meltwater sediments. *Chem. Geol.* **218**, 203–221 (2005).
74. N. Kumar, J. L. Pacheco, V. Noël, G. Dublet, G. E. Brown, Sulfidation mechanisms of Fe(III)-(oxyhydr)oxide nanoparticles: a spectroscopic study. *Environ. Sci. Nano.* **5**, 1012–1026 (2018).
75. P. Liao, S. Yuan, D. Wang, Impact of Redox Reactions on Colloid Transport in Saturated Porous Media: An Example of Ferrihydrite Colloids Transport in the Presence of Sulfide. *Environ. Sci. Technol.* **50**, 10968–10977 (2016).
76. S. Katsev, B. Sundby, A. Mucci, Modeling vertical excursions of the redox boundary in sediments: Application to deep basins of the Arctic Ocean. *Limnol. Oceanogr.* **51**, 1581–1593 (2006).

77. C. Gagnon, A. Mucci, É. Pelletier, Vertical distribution of dissolved sulphur species in coastal marine sediments. *Mar. Chem.* **52**, 195–209 (1996).
78. O. M. Suleimenov, T. M. Seward, A spectrophotometric study of hydrogen sulphide ionisation in aqueous solutions to 350°C. *Geochim. Cosmochim. Acta.* **61**, 5187–5198 (1997).
79. D. C. Nelson, J. Amend, K. Edwards, T. Lyons, Sulfide oxidation in marine sediments: geochemistry meets microbiology. *Spec. Pap. 379 Sulfur Biogeochem.-Past Present*, 63–81 (2004).
80. M. Dos Santos Afonso, W. Stumm, Reductive dissolution of iron (III)(hydr) oxides by hydrogen sulfide. *Langmuir*. **8**, 1671–1675 (1992).
81. W. Yao, F. J. Millero, Oxidation of hydrogen sulfide by hydrous Fe(III) oxides in seawater. *Mar. Chem.* **52**, 1–16 (1996).
82. M. Eigen, R. Wilkins, The kinetics and mechanism of formation of metal complexes. *Mech. Inorg. React.* **49**, 55–67 (1965).
83. D. Rickard, Kinetics of FeS precipitation: Part 1. Competing reaction mechanisms. *Geochim. Cosmochim. Acta.* **59**, 4367–4379 (1995).
84. G. W. Luther, D. T. Rickard, Metal Sulfide Cluster Complexes and their Biogeochemical Importance in the Environment. *J. Nanoparticle Res.* **7**, 389–407 (2005).
85. D. Wei, K. Osseo-Asare, Formation of Iron Monosulfide: A Spectrophotometric Study of the Reaction between Ferrous and Sulfide Ions in Aqueous Solutions. *J. Colloid Interface Sci.* **174**, 273–282 (1995).
86. J. Buffe, R. De Vitre, D. Perret, G. Leppard, Combining Field Measurements for Speciation in Non Perturbable Water Samples: Application to the Iron and Sulfide Cycles in a Eutrophic Lake. *Met. Speciat. Theory Anal. Appl. Lewis Publ. Chelsea Mich. 1988 P 99-124 9 Fig 25 Ref* (1988).
87. S. M. Theberge, G. W. Luther, A. M. Farrenkopf, On the existence of free and metal complexed sulfide in the Arabian Sea and its oxygen minimum zone. *Deep Sea Res. Part II Top. Stud. Oceanogr.* **44**, 1381–1390 (1997).
88. J. W. Morse, H. Thomson, D. W. Finneran, Factors Controlling Sulfide Geochemistry in Sub-tropical Estuarine and Bay Sediments. *Aquat. Geochem.* **13**, 143–156 (2007).
89. D. Rickard, The solubility of FeS. *Geochim. Cosmochim. Acta.* **70**, 5779–5789 (2006).
90. M. T. Hurtgen, T. W. Lyons, E. D. Ingall, A. M. Cruse, Anomalous enrichments of iron monosulfide in euxinic marine sediments and the role of H₂S in iron sulfide transformations; examples from Effingham Inlet, Orca Basin, and the Black Sea. *Am. J. Sci.* **299**, 556–588 (1999).
91. S. Smith, J. Hollibaugh, Coastal metabolism and the oceanic organic carbon balance. *Rev. Geophys.* **31**, 75–89 (1993).

92. R.-M. Couture, R. Fischer, P. Van Cappellen, C. Gobeil, Non-steady state diagenesis of organic and inorganic sulfur in lake sediments. *Geochim. Cosmochim. Acta.* **194**, 15–33 (2016).
93. D. Blomstrom, E. Knight Jr, W. Phillips, J. Weiher, The nature of iron in ferredoxin. *Proc. Natl. Acad. Sci. U. S. A.* **51**, 1085 (1964).
94. E. D. Burton, R. T. Bush, S. G. Johnston, L. A. Sullivan, A. F. Keene, Sulfur biogeochemical cycling and novel Fe–S mineralization pathways in a tidally re-flooded wetland. *Geochim. Cosmochim. Acta.* **75**, 3434–3451 (2011).
95. J. P. Werne, D. J. Hollander, T. W. Lyons, J. S. Damsté, Organic sulfur biogeochemistry: recent advances and future research directions. *Spec. Pap.-Geol. Soc. Am.*, 135–150 (2004).
96. M. Wolthers, L. Charlet, P. R. van Der Linde, D. Rickard, C. H. van Der Weijden, Surface chemistry of disordered mackinawite (FeS). *Geochim. Cosmochim. Acta.* **69**, 3469–3481 (2005).
97. F. M. Michel *et al.*, Short- to Medium-Range Atomic Order and Crystallite Size of the Initial FeS Precipitate from Pair Distribution Function Analysis. *Chem. Mater.* **17**, 6246–6255 (2005).
98. R. B. Herbert, S. G. Benner, A. R. Pratt, D. W. Blowes, Surface chemistry and morphology of poorly crystalline iron sulfides precipitated in media containing sulfate-reducing bacteria. *Chem. Geol.* **144**, 87–97 (1998).
99. A. R. Lennie, S. A. T. Redfern, P. F. Schofield, D. J. Vaughan, Synthesis and Rietveld crystal structure refinement of mackinawite, tetragonal FeS. *Mineral. Mag.* **59**, 677–683 (1995).
100. W. Fischer, U. Schwertmann, The Formation of Hematite from Amorphous Iron(III) Hydroxide. *Clays Clay Min.* **23**, 33–37 (1974).
101. D. Rickard, I. B. Butler, A. Oldroyd, A novel iron sulphide mineral switch and its implications for Earth and planetary science. *Earth Planet. Sci. Lett.* **189**, 85–91 (2001).
102. D. Rickard, Kinetics of pyrite formation by the H₂S oxidation of iron (II) monosulfide in aqueous solutions between 25 and 125°C: The rate equation. *Geochim. Cosmochim. Acta.* **61**, 115–134 (1997).
103. B. M. Toner *et al.*, Preservation of iron (II) by carbon-rich matrices in a hydrothermal plume. *Nat. Geosci.* **2**, 197 (2009).
104. N. K. Niazi, E. D. Burton, Arsenic sorption to nanoparticulate mackinawite (FeS): An examination of phosphate competition. *Environ. Pollut.* **218**, 111–117 (2016).
105. H. Y. Jeong, B. Klaue, J. D. Blum, K. F. Hayes, Sorption of Mercuric Ion by Synthetic Nanocrystalline Mackinawite (FeS). *Environ. Sci. Technol.* **41**, 7699–7705 (2007).
106. D. S. Han, B. Batchelor, A. Abdel-Wahab, Sorption of selenium(IV) and selenium(VI) to mackinawite (FeS): Effect of contact time, extent of removal, sorption envelopes. *J. Hazard. Mater.* **186**, 451–457 (2011).

107. A. Picard, A. Gartman, D. R. Clarke, P. R. Girguis, Sulfate-reducing bacteria influence the nucleation and growth of mackinawite and greigite. *Geochim. Cosmochim. Acta.* **220**, 367–384 (2018).
108. A. Picard, A. Gartman, P. R. Girguis, What Do We Really Know about the Role of Microorganisms in Iron Sulfide Mineral Formation? *Front. Earth Sci.* **4** (2016), doi:10.3389/feart.2016.00068.
109. A. Picard, D. Testemale, L. Wagenknecht, R. Hazael, I. Daniel, Iron reduction by the deep-sea bacterium *Shewanella profunda* LT13a under subsurface pressure and temperature conditions. *Front. Microbiol.* **5** (2015), doi:10.3389/fmicb.2014.00796.
110. R. Dufour, P. Ouellet, Maurice Lamontagne Institute, *Estuary and Gulf of St. Lawrence marine ecosystem overview and assessment report* (Dept. of Fisheries and Oceans, Maurice-Lamontagne Institut, Mont-Joli, Québec, 2007).
111. C. Gagnon, A. Mucci, É. Pelletier, Anomalous accumulation of acid-volatile sulphides (AVS) in a coastal marine sediment, Saguenay Fjord, Canada. *Geochim. Cosmochim. Acta.* **59**, 2663–2675 (1995).
112. H. M. Edenborn, N. Silverberg, A. Mucci, B. Sundby, Sulfate reduction in deep coastal marine sediments. *Mar. Chem.* **21**, 329–345 (1987).
113. H. M. Edenborn *et al.*, A glove box for the fine-scale subsampling of sediment box cores. *Sedimentology*. **33**, 147–150 (1986).
114. J. D. Cline, Spectrophotometric Determination of Hydrogen Sulfide in Natural Waters. *Limnol. Oceanogr.* **14**, 454–458 (1969).
115. R. T. Sheen, H. L. Kahler, E. M. Ross, W. H. Betz, L. D. Betz, Turbidimetric Determination of Sulfate in Water. *Ind. Eng. Chem. Anal. Ed.* **7**, 262–265 (1935).
116. L. S. Clesceri *et al.*, *Standard methods for the examination of water and wastewater* (American Public Health Association, Washington, DC, 1989).
117. D. Rickard, J. W. Morse, Acid volatile sulfide (AVS). *Mar. Chem.* **97**, 141–197 (2005).
118. G. W. Luther, Acid volatile sulfide—a comment. *Mar. Chem.* **97**, 198–205 (2005).
119. F. J. R. Meysman, J. J. Middelburg, Acid-volatile sulfide (AVS) — A comment. *Mar. Chem.* **97**, 206–212 (2005).
120. D. Rickard, J. Morse, Acid volatile sulfide: Authors' closing comments. *Mar. Chem.* **97**, 213–215 (2005).
121. I. Langmuir, The Adsorption of Gases on Plane Surfaces of Glass, Mica, and Platinum. *J. Am. Chem. Soc.* **40**, 1361–1403 (1918).
122. A. W. Adamson, A. P. Gast, *Physical chemistry of surfaces* (Wiley, 1997; <https://books.google.ca/books?id=rK4PAQAAQAAJ>).

123. H. Freundlich, Über die Adsorption in Lösungen. *Z. Für Phys. Chem.* **57U**, 385–470 (1907).
124. T. A. Davis, B. Volesky, A. Mucci, A review of the biochemistry of heavy metal biosorption by brown algae. *Water Res.* **37**, 4311–4330 (2003).
125. J. C. Y. Ng, W. H. Cheung, G. McKay, Equilibrium Studies of the Sorption of Cu(II) Ions onto Chitosan. *J. Colloid Interface Sci.* **255**, 64–74 (2002).
126. K. Vasanth Kumar, S. Sivanesan, Isotherms for Malachite Green onto rubber wood (*Hevea brasiliensis*) sawdust: Comparison of linear and non-linear methods. *Dyes Pigments.* **72**, 124–129 (2007).
127. O. Redlich, D. L. Peterson, A Useful Adsorption Isotherm. *J. Phys. Chem.* **63**, 1024–1024 (1959).
128. K. Y. Foo, B. H. Hameed, Insights into the modeling of adsorption isotherm systems. *Chem. Eng. J.* **156**, 2–10 (2010).
129. R. Andrae, T. Schulze-Hartung, P. Melchior, Dos and don'ts of reduced chi-squared. *ArXiv Prepr. ArXiv10123754* (2010).
130. K. Lalonde, A. Mucci, A. Ouellet, Y. Gélinas, Preservation of organic matter in sediments promoted by iron. *Nature.* **483**, 198–200 (2012).
131. K. Heymann, J. Lehmann, D. Solomon, M. W. I. Schmidt, T. Regier, C 1s K-edge near edge X-ray absorption fine structure (NEXAFS) spectroscopy for characterizing functional group chemistry of black carbon. *Org. Geochem.* **42**, 1055–1064 (2011).
132. J. A. Brandes *et al.*, Examining marine particulate organic matter at sub-micron scales using scanning transmission X-ray microscopy and carbon X-ray absorption near edge structure spectroscopy. *Mar. Chem.* **92**, 107–121 (2004).
133. J. A. Tossell, D. J. Vaughan, K. H. Johnson, The Electronic Structure of Rutile, Wustite, and Hematite from Molecular Orbital Calculations. *Am. Mineral.* **59**, 319–334 (1974).
134. G. A. Waychunas, M. J. Apted, G. E. Brown, X-ray K-edge absorption spectra of Fe minerals and model compounds: Near-edge structure. *Phys. Chem. Miner.* **10**, 1–9 (1983).
135. J. Kinyangi *et al.*, Nanoscale Biogeocomplexity of the Organomineral Assemblage in Soil. *Soil Sci. Soc. Am. J.* **70**, 1708–1718 (2006).
136. L. Remusat *et al.*, NanoSIMS Study of Organic Matter Associated with Soil Aggregates: Advantages, Limitations, and Combination with STXM. *Environ. Sci. Technol.* **46**, 3943–3949 (2012).
137. J. Wan, T. Tyliszczak, T. K. Tokunaga, Organic carbon distribution, speciation, and elemental correlations within soil microaggregates: Applications of STXM and NEXAFS spectroscopy. *Geochim. Cosmochim. Acta.* **71**, 5439–5449 (2007).
138. M. Keiluweit *et al.*, Nano-scale investigation of the association of microbial nitrogen residues with iron (hydr)oxides in a forest soil O-horizon. *Geochim. Cosmochim. Acta.* **95**, 213–226 (2012).

139. D. Richard, B. Sundby, A. Mucci, Kinetics of manganese adsorption, desorption, and oxidation in coastal marine sediments. *Limnol. Oceanogr.* **58**, 987–996 (2013).
140. D. Burdige, J. Gieskes, A Pore Water/Solid Phase Diagenetic Model for Manganese in Marine Sediments. *Am. J. Sci.* (1983), doi:10.2475/ajs.283.1.29.
141. B. Sundby, N. Silverberg, R. Chesselet, Pathways of manganese in an open estuarine system. *Geochim. Cosmochim. Acta.* **45**, 293–307 (1981).
142. D. E. Canfield, Reactive iron in marine sediments. *Geochim. Cosmochim. Acta.* **53**, 619–632 (1989).
143. D. E. Canfield, R. Raiswell, S. H. Bottrell, The reactivity of sedimentary iron minerals toward sulfide. *Am. J. Sci.* **292**, 659–683 (1992).
144. F. Gimbert, N. Morin-Crini, F. Renault, P.-M. Badot, G. Crini, Adsorption isotherm models for dye removal by cationized starch-based material in a single component system: Error analysis. *J. Hazard. Mater.* **157**, 34–46 (2008).
145. G. Heron, C. Crouzet, A. C. M. Bourg, T. H. Christensen, Speciation of Fe(II) and Fe(III) in Contaminated Aquifer Sediments Using Chemical Extraction Techniques. *Environ. Sci. Technol.* **28**, 1698–1705 (1994).
146. N. R. J. Poolton, I. W. Kirkman, E. Pantos, On the role of Fe²⁺ in the luminescence of feldspar: an exploration of Fe²⁺/Fe³⁺ L-edge near edge x-ray absorption fine structure using comparative electronic and optical detection methods. *J. Phys. Appl. Phys.* **44**, 485402 (2011).
147. M. Womes *et al.*, Electronic Structures of FeS and FeS₂: X-Ray Absorption Spectroscopy and Band Structure Calculations. *J. Phys. Chem. Solids.* **58**, 345–352 (1997).
148. J. Lehmann *et al.*, in *Biophysico-Chemical Processes Involving Natural Nonliving Organic Matter in Environmental Systems* (John Wiley & Sons, Ltd, 2009); <https://onlinelibrary.wiley.com/doi/abs/10.1002/9780470494950.ch17>, pp. 729–781.
149. N. Hertkorn *et al.*, Characterization of a major refractory component of marine dissolved organic matter. *Geochim. Cosmochim. Acta.* **70**, 2990–3010 (2006).
150. J. I. Hedges, R. G. Keil, R. Benner, What happens to terrestrial organic matter in the ocean? *Org. Geochem.* **27**, 195–212 (1997).
151. M. McCarthy, T. Pratum, J. Hedges, R. Benner, Chemical composition of dissolved organic nitrogen in the ocean. *Nature.* **390**, 150–154 (1997).
152. Y. K. Henneberry, T. E. C. Kraus, P. S. Nico, W. R. Horwath, Structural stability of coprecipitated natural organic matter and ferric iron under reducing conditions. *Org. Geochem.* **48**, 81–89 (2012).
153. J. I. Hedges *et al.*, The molecularly-uncharacterized component of nonliving organic matter in natural environments. *Org. Geochem.* **31**, 945–958 (2000).

154. B. Subramanyam, A. Das, Linearized and non-linearized isotherm models comparative study on adsorption of aqueous phenol solution in soil. *Int. J. Environ. Sci. Technol.* **6**, 633–640 (2009).
155. B. Ransom, R. H. Bennett, R. Baerwald, K. Shea, TEM study of in situ organic matter on continental margins: occurrence and the “monolayer” hypothesis. *Mar. Geol.* **138**, 1–9 (1997).
156. L. Mayer, Extent of coverage of mineral surfaces by organic matter in marine sediments. *Geochim. Cosmochim. Acta*. **63**, 207–215 (1999).
157. D. J. Mackey, A. Zirino, Comments on trace metal speciation in seawater or do “onions” grow in the sea? *Anal. Chim. Acta*. **284**, 635–647 (1994).
158. M. Baalousha, A. Manculea, S. Cumberland, K. Kendall, J. R. Lead, Aggregation and surface properties of iron oxide nanoparticles: Influence of pH and natural organic matter. *Environ. Toxicol. Chem.* **27**, 1875–1882 (2008).
159. X. Châtellier *et al.*, Characterization of Iron-Oxides Formed by Oxidation of Ferrous Ions in the Presence of Various Bacterial Species and Inorganic Ligands. *Geomicrobiol. J.* **21**, 99–112 (2004).
160. E. Breitbarth *et al.*, Iron biogeochemistry across marine systems—progress from the past decade. *Biogeosciences*. **7**, 1075–1097 (2010).
161. E. Tipping, C. Rey-Castro, S. E. Bryan, J. Hamilton-Taylor, Al (III) and Fe (III) binding by humic substances in freshwaters, and implications for trace metal speciation. *Geochim. Cosmochim. Acta*. **66**, 3211–3224 (2002).
162. G. R. Aiken, H. Hsu-Kim, J. N. Ryan, Influence of Dissolved Organic Matter on the Environmental Fate of Metals, Nanoparticles, and Colloids. *Environ. Sci. Technol.* **45**, 3196–3201 (2011).
163. P. L. Croot *et al.*, Retention of dissolved iron and Fe II in an iron induced Southern Ocean phytoplankton bloom. *Geophys. Res. Lett.* **28**, 3425–3428 (2001).
164. E. J. O'Loughlin, C. A. Gorski, M. M. Scherer, M. I. Boyanov, K. M. Kemner, Effects of Oxyanions, Natural Organic Matter, and Bacterial Cell Numbers on the Bioreduction of Lepidocrocite (γ -FeOOH) and the Formation of Secondary Mineralization Products. *Environ. Sci. Technol.* **44**, 4570–4576 (2010).
165. J. Cosmidis, C. W. Nims, D. Diercks, A. S. Templeton, Formation and stabilization of elemental sulfur through organomineralization. *Geochim. Cosmochim. Acta*. **247**, 59–82 (2019).
166. E. D. Burton *et al.*, Iron-monosulfide oxidation in natural sediments: resolving microbially mediated S transformations using XANES, electron microscopy, and selective extractions. *Environ. Sci. Technol.* **43**, 3128–3134 (2009).
167. R. Pocklington, J. Leonard, Terrigenous organic matter in sediments of the St. Lawrence Estuary and the Saguenay Fjord. *J. Fish. Board Can.* **36**, 1250–1255 (1979).
168. D. Large, N. Fortey, A. Milodowski, A. Christy, J. Dodd, Petrographic observations of iron, copper, and zinc sulfides in freshwater canal sediment. *J. Sediment. Res.* **71**, 61–69 (2001).

169. R. A. Berner, Burial of organic carbon and pyrite sulfur in the modern ocean; its geochemical and environmental significance. *Am. J. Sci.* **282**, 451–473 (1982).